Statistical Modeling of Gas-Phase Organometallic Reactions Based on Density Functional Theory: $Ni^+ + C_3H_8$

Sung Soo Yi,[†] Margareta R. A. Blomberg,*[,‡] Per E. M. Siegbahn,[‡] and James C. Weisshaar*[,†]

Department of Chemistry, University of Wisconsin—Madison, Madison, Wisconsin, 53706-1396, and Department of Physics, University of Stockholm, Box 6730, S-113 85, Stockholm, Sweden

Received: August 13, 1997; In Final Form: October 21, 1997[⊗]

Density functional theory in its B3LYP variant has been used to explore quantitative details of the adiabatic potential energy surface leading from $Ni^+ + C_3H_8$ reactants through a deep $Ni^+(C_3H_8)$ well to $NiC_2H_4^+ + CH_4$ and $NiC_3H_6^+ + H_2$ elimination products. The lowest energy path to CH_4 elimination involves facile CC bond insertion followed by a high *multicenter transition state* (MCTS) leading directly to the exit-channel complex $Ni^+(C_2H_4)(CH_4)$. The lowest energy path to H_2 elimination involves comparably facile *secondary* CH insertion followed by a comparably high MCTS leading directly to the $Ni^+(C_3H_6)(H_2)$ complex. Primary CH insertion leads to significantly higher barriers to both CH_4 and H_2 elimination; in particular, β-methyl migration is energetically very costly. These results support a mechanism significantly different from the stepwise mechanisms invoked earlier but the same as that found in recent calculations on the $Fe^+ + C_3H_8$ reaction by Holthausen and Koch. The geometries suggest that agostic interactions are important in stabilizing the key MCTSs. We use the B3LYP geometry (moments of inertia) and harmonic vibrational frequencies at each stationary point to construct a detailed rate model of the reaction, applying RRKM theory to each reaction step on the adiabatic ground-state surface. A steady-state approximation holds well and leads to a simple parallel decay model for the long-lived $Ni^+(C_3H_8)$ complexes. By adjusting the energies of the key MCTSs downward by 5−7 kcal/mol from the values from B3LYP theory, we can explain the range of experimental time scales, the product branching fractions, total cross section vs kinetic energy, and deuterium isotope effects. Differential centrifugal effects arising from the substantial variation of the mass distribution along the reaction coordinates lead to a strong *J*-dependence of the $Ni^+(C_3H_8)$ decay rate and of product branching fractions as well. The resulting mechanistic picture indicates that at low energy only low-*J* complexes (formed at small impact parameter) can overcome the centrifugal barriers atop the MCTSs and produce elimination products. High-*J* complexes live as $Ni^+(C_3H_8)$ for nanoseconds−microseconds, repeatedly insert in CC and CH bonds, but eventually revert to $Ni^+ + C_3H_8$ reactants. We suggest possible reasons why the new model *cannot* explain the bimodal kinetic energy release distribution observed by Bowers and co-workers in the $NiC_3H_6^+ + H_2$ channel.

I. Introduction

In the coming decade, electronic structure theory may begin to make real contributions to the rational design of organometallic catalysts by suggesting strategies for lowering key barriers along reaction paths. Already theory is able to provide useful quantitative energetic information for quite large, electronically complicated organometallic species.[1] Particularly noteworthy are the scaled configuration interaction theory known as PCI-80[2] and the density functional theory in its B3LYP formulation.[3] Both of these methods can treat remarkably large systems. For simple ligated transition-metal species such as gas-phase MH^+ and MCH_3^+, careful comparisons show that in most cases PCI-80 and B3LYP can compute bond energies to an accuracy of 3−5 kcal/mol, which is comparable to the experimental accuracy.[4]

A more difficult question is how well theory can compute the energies of key reaction intermediates and especially of *transition states*, since barrier heights typically dictate reaction rates and product branching. The chemistry of gas-phase transition-metal atoms, both neutral and cationic, provides many excellent model systems on which to carry out such tests. The bare transition-metal cations are remarkable for their ability to react with small alkanes at room temperature to break CH and CC bonds and eliminate H_2 or a small alkane.[5] For *neutral* transition-metal atoms M, we have carried out an extended series of measurements of gas-phase reaction rates with small alkanes and alkenes at 300 K.[6,7] In the 4d series, a parallel set of PCI-80 calculations were in good agreement with experimental results, in the sense that only small theoretical barriers (less than about 5 kcal/mol) were found for those reactions observed to occur at 300 K, while large barriers in excess of about 10 kcal/mol were found for M + hydrocarbon pairs that do not react.[7]

In this paper, we combine B3LYP electronic structure calculations with statistical rate theory to model the $Ni^+ + C_3H_8$ reaction, which was studied in a crossed-beam experiment described in the preceding paper 1.[8] The $Ni^+ + C_3H_8$ reaction and its Fe^+ and Co^+ counterparts have become experimental benchmarks in the sense that they have been studied by essentially the entire arsenal of mass spectrometric and ion beam

* To whom correspondence should be addressed. E-mail addresses weisshaar@chem.wisc.edu,mb@physto.SE.

⊗ Abstract published in *Advance ACS Abstracts,* December 15, 1997.

S1089-5639(97)02674-1 CCC: $15.00 © 1998 American Chemical Society
Published on Web 01/08/1998

techniques. The standard mechanism has invoked initial, rate-limiting CH or CC insertion by the metal atom, subsequent β-hydrogen or β-alkyl migration to the metal, and three-center elimination of H_2 or CH_4.[9−11] In contrast, theory is finding *low* barriers to the initial CH or CC insertion intermediate.[12−14] The highest potential energy along paths to H_2 and CH_4 elimination occurs at intriguing *multicenter transition states* (MCTSs). These involve concerted motion of *many* atoms along a segment of the reaction path connecting each insertion intermediate to the corresponding exit-channel ion-induced-dipole complex.[15] It appears that these MCTSs may be unique to transition-metal *cation* chemistry.

The goal of this paper is to combine realistic energies, geometries, and vibrational frequency sets from density functional theory for all key reaction intermediates and transition states to build a detailed statistical rate model for the $Ni^+ + C_3H_8$ reaction. The model provides absolute time scales for complex fragmentation and time-dependent branching fractions that are directly comparable to our experiments (paper 1) and those of other groups. By exploring modest variations in the details of the statistical model, the frequency sets, and the energetics of key intermediates and TSs, we can achieve remarkably good agreement with a variety of experiments. The angular momentum deposited in the collision complex as orbital angular momentum plays a fascinating role in the dynamics due to changes in the moments of inertia, and thus effective barrier heights, during the course of the reaction. Closely analogous effects have recently been studied in bimolecular reactions of smaller neutral systems by Troe[16] and in a variety of unimolecular dissociation reactions by Hase[17] and Baer.[18] We conclude by using our new model with angular momentum constraints to speculate on a possible explanation for the anomalous, nonstatistical H_2 kinetic energy release distributions (KERDs) observed in reactions of Fe^+, Co^+, and Ni^+ with C_3H_8.[10,11]

II. Overview of the Model

The new model of the $Ni^+ + C_3H_8$ reaction is based on the mechanisms indicated by the present calculations and by recent calculations on Fe^+ and Co^+ as well.[12−14] The model includes formation of the long-lived ion-induced-dipole complex **1** in the entrance channel (Figure 1), which subsequently decays into three parallel channels: dissociation back to reactants (k_{diss}); CC bond insertion to intermediate **2**, leading to eventual CH_4 elimination (k_{CH_4}); and *secondary* CH bond insertion to intermediate **4**, leading to eventual H_2 elimination (k_{H_2}). Figure 1a,b shows key intermediates and transition states along the two postulated elimination paths. There is also a deep ion-induced-dipole complex for each exit channel, **3** for the CH_4 channel, and **5** for the H_2 elimination channel.

Our detailed kinetics model (Figure 2) for the decay of $Ni(C_3H_8)^+$ complexes **1** includes the dissociation rate k_{diss} across the entrance-channel "orbiting transition state" $\mathbf{TS_{orb}}$, forward and reverse rates k_{CC} and k_{-CC} across the CC insertion transition state $\mathbf{TS_{CC}}$, forward and reverse rates k_{CH} and k_{-CH} across the *secondary* CH insertion transition state $\mathbf{TS_{CH}(2°)}$, and forward and reverse rates $k_{MC}^{CH_4}$, k_{32} and $k_{MC}^{H_2}$, k_{54} across the *multicenter transition states* $\mathbf{MCTS}_{CH_4}$ and $\mathbf{MCTS}_{H_2}(\mathbf{2°})$, respectively. For realistic energies, the reverse rates k_{32} and k_{54} across $\mathbf{MCTS}_{CH_4}$ and $\mathbf{MCTS}_{H_2}$ are too slow to compete with the final elimination rates k_3^{exit} and k_5^{exit} from **3** and **5** across $\mathbf{TS_{orb}}'$ and $\mathbf{TS_{orb}}''$. We explored pathways beginning with *primary* CH insertion but found substantially larger barriers to both H_2 and CH_4 elimination than for the paths described above. All forward and reverse

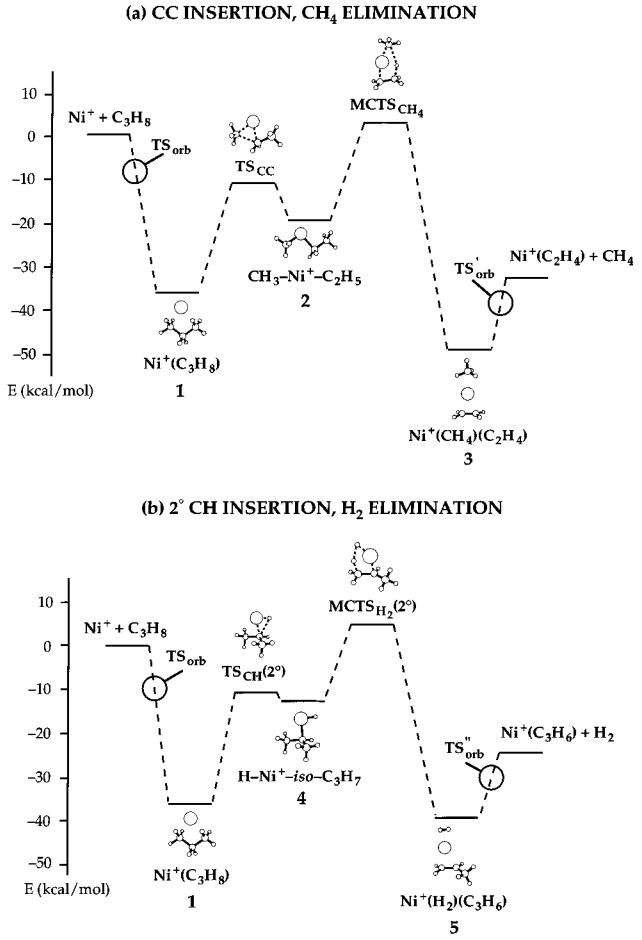

Figure 1. Potential wells and transition states along two parallel paths to elimination (a) of CH_4 and (b) of H_2. Energies are calculated from B3LYP theory and corrected for zero-point effects. See Table 1 for quantitative energetics.

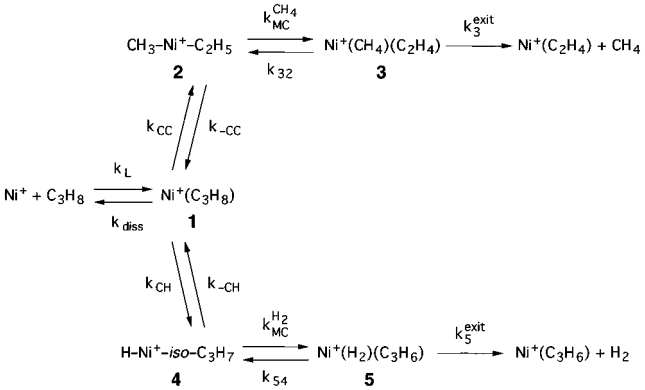

Figure 2. Detailed parallel kinetics model for decay of $Ni^+(C_3H_8)$ complexes **1** backward to reactants or forward to CH_4 or H_2 elimination products.

microcanonical rates $k_i(E,J)$ will be calculated from RRKM theory,[19−21] a particular variant of unimolecular-transition state theory, as a function of total energy E and angular momentum J. These rates are then combined to build the overall kinetics model for the decay of the complex.

For many years, it had been postulated that the *rate-limiting step* in M^+ + alkane reactions was initial CH or CC bond insertion, followed by facile β-H or β-alkyl migration to the metal atom to form stable intermediates of the form $M^+(H)_2$(alkene) or $M^+(H)(R)$(alkene′), and subsequent elimination of H_2 or of a smaller alkane.[9−11] For $M^+ + C_3H_8$, initial CH

insertion almost surely leads to the H_2 product, but it has been difficult to discern from experiment whether initial CH or CC insertion (or both) leads to CH_4 elimination. Recent theoretical work on $Fe^+ + C_2H_6$ and C_3H_8, $Co^+ + C_2H_6$,[12−14] and now $Ni^+ + C_3H_8$ calls into question the very existence of stable minima of the form $M^+(H)_2$(alkene) or $M^+(H)(CH_3)$(alkene). Instead, both DFT and PCI-80 calculations are finding *multicenter transition states* (MCTSs) connecting the CH insertion intermediate directly to the exit-channel complex of the form $M^+(H_2)$(alkene) and the CC insertion intermediate directly to $M^+(CH_4)(C_2H_4)$, as in Figure 1. At least for cationic systems, the importance of such transition states may be due in part to agostic interactions,[22] as discussed by Holthausen and Koch.[12−14] These transition states are evidently the highest points on the lowest energy paths to H_2 or CH_4 elimination. For Ni^+ insertion into a *primary* CH bond of propane, we will find a significantly *higher* MCTS leading toward H_2 elimination, perhaps partly due to the absence of stabilizing agostic interactions. In addition, following primary CH insertion we find even larger barriers to *β-methyl* migration than to *β-hydrogen* migration. Theory thus makes a clear prediction that for $Ni^+ + C_3H_8$ at low energy CH_4 elimination occurs exclusively by initial CC bond insertion and H_2 elimination occurs exclusively by initial *secondary* CH bond insertion.

As always, our statistical model assumes that reaction occurs on a single adiabatic potential energy surface, despite the large number of low-lying electronic states of reactants and presumably of intermediates as well. We make the standard RRKM assumption of no recrossing trajectories that would cause statistical rate theory to overestimate microscopic rates. Compared with earlier modeling efforts,[10,11] we have the advantage of realistic information about vibrational frequencies and geometries (moments of inertia) at key stationary points from density functional theory.

III. Electronic Structure Calculations: $Ni^+ + C_3H_8$

In this section we briefly describe the electronic structure calculations from which we build the rate model. First, the stationary points are located using B3LYP, a density functional theory (DFT) based on hybrid functionals. In the B3LYP geometry optimizations the LANL2DZ set of the Gaussian-94 program[23] is used. For the nickel atom a nonrelativistic effective core potential (ECP) according to Hay and Wadt[24a] together with a valence basis set of essentially double-ζ quality including a diffuse 3d function is used. For the other atoms Dunning/Huzinaga double-ζ basis sets are used.[24b] In each structure obtained in this way (minimum or transition state) an energy calculation is performed at the B3LYP level using the large basis set 6-311+G(2d,2p) in the Gaussian-94 program. This basis set includes the Wachters[25] all-electron basis on nickel, two sets of polarization functions on all atoms including two f-functions on nickel (with exponents 2.58 and 0.645), and also diffuse functions. All relative energies reported are based on the results for this large basis.

The DFT calculations were made using the empirically parametrized B3LYP functional:[3]

$$F\{\mathrm{B3LYP}\} = (1-A)F_x^{\mathrm{Slater}} + AF_x^{\mathrm{HF}} + BF_x^{\mathrm{Becke}} + CF_c^{\mathrm{LYP}} + (1-C)F_c^{\mathrm{VWN}} \quad (1)$$

where F_x^{Slater} is the Slater exchange, F_x^{HF} is the Hartree−Fock exchange, F_x^{Becke} is the gradient part of the Becke functional,[3] F_c^{LYP} is the correlation functional of Lee, Yang, and Parr,[26] and F_c^{VWN} is the correlation functional of Vosko, Wilk, and Nusair.[27] *A*, *B*, and *C* are the coefficients determined by Becke[3] from a fit to experimental heats of formation for a benchmark test[28] consisting of 55 first- and second-row molecules. However, it should be noted that Becke did not use F_c^{LYP} and F_c^{VWN} in the expression above when the coefficients were determined, but used the correlation functionals of Perdew and Wang instead.[29]

TABLE 1: Calculated Reaction Path Energetics for $Ni^+ + C_3H_8$ and $Ni^+ + C_3D_8$ from Density Functional Theory (B3LYP)[a]

species	ΔE_H	ΔE_D	species	ΔE_H	ΔE_D
$Ni^+ + C_3H_8$	0	0	Ni(H)(*iso*-C_3H_7)$^+$	−11.6	−10.6
$Ni(C_3H_8)^+$	−35.6	−35.8	**MCTS**$_{H_2}$ (2°)	+5.0	+7.0
TS$_{CC}$	−10.5	−10.1	$Ni(H_2)(C_3H_6)^+$ [c]	−38.7	−37.0
$Ni(CH_3)(C_2H_5)^+$	−19.0	−18.5	$NiC_3H_6^+ + H_2$[d]	−23.6	−21.4
MCTS$_{CH_4}$	+3.1	+4.6	**TS**$_{CH}$ (1°)	−9.4	−8.3
$Ni(CH_4)(C_2H_4)^+$	−48.7	−48.0	Ni(H)(*n*-C_3H_7)$^+$	−9.4	−8.6
$NiC_2H_4^+ + CH_4$[b]	−33.3	−32.7	**MCTS**$_{H_2}$ (1°)	+11.4	+13.3
TS$_{CH}$ (2°)	−11.0	−9.9	**MCTS**$_{CH_4}$ (1°)	+16.8	+18.4

[a] Species refer to Figure 1 and text. All energies in kcal/mol relative to ground-state reactants and including differential zero-point energy corrections. ΔE_H refers to $Ni^+ + C_3H_8$; ΔE_D refers to $Ni^+ + C_3D_8$. [b] Experimental estimate of exothermicity: -27.0 ± 1.2 kcal/mol (ref 32). [c] Geometry optimization incomplete; complex includes one imaginary frequency of 134i cm^{-1}. [d] Experimental estimate of exothermicity: -17.3 ± 2.3 kcal/mol (ref 32).

Zero-point vibrational energies were determined for all stationary points as follows. At each optimized stationary point the force-constant matrix was calculated to determine the character of the stationary points (minima or transition states) and also to evaluate the zero-point vibrational energy corrections, which are included in all relative energies. The calculations of the force constants were performed at the B3LYP level using essentially double-ζ quality basis sets. For the nickel atom the Wachters[25] all-electron basis set was used. The smallest vibrational frequencies (below 100 cm^{-1}) are uncertain due to a variety of technical factors. First, the basis set used in the geometry optimization and frequency calculations differ. Second, the SCF convergence is sometimes imperfect, and the forces are calculated on a grid of finite mesh size. Thus, the separation between vibration and rotation/translation is imperfect. In the rate calculations described below, we explore the possible effects of this uncertainty in low frequencies and find that the key quantitative conclusions regarding barrier heights from the rate modeling are not greatly affected.

A difficulty in the calculation of relative energies involving transition-metal atoms is that atomic spectra are seldom well reproduced by theory. In particular, B3LYP often overestimates the stability of atomic $3d^x$ configurations relative to $3d^{x-1}4s$. For Ni^+, this is a very mild effect. The energy difference between the $3d^84s(^4F)$ excited state and the $3d^9(^2D)$ ground state as calculated in the present study is 28.6 kcal/mol, only 3.7 kcal/mol higher than the experimental difference in $(2J_{el}+1)$-weighted energies of 24.9 kcal/mol. The error is small partly due to cancellation, since relativistic contributions are neglected. Ricca and Baushlicher[30] have suggested a scheme for correcting for errors in the atomic spectra when calculating the energetics of molecular species by interpolation between atomic asymptotes based on the 3d population of the metal atom in the molecule. We have followed their scheme in this work, but the largest resulting correction is only 1.2 kcal/mol.

The B3LYP energetic results are summarized in Table 1, where the names of potential wells and transition states refer to Figure 1. For each species, we give the energy relative to

TABLE 2: Vibrational Frequencies (cm^{-1}) Used in RRKM Calculations for $Ni^+ + C_3H_8$ Reaction[a]

1	2	TS_{CC}	$MCTS_{CH_4}$	4	$TS_{CH}(2°)$	$MCTS_{H_2}(2°)$
3154	3234	3248	3248	3189	3185	3220
3130	3224	3242	3218	3149	3151	3185
3126	3172	3157	3209	3132	3134	3173
3090	3132	3143	3129	3087	3088	3113
3033	3122	3136	3117	3074	3078	3093
3022	3069	3062	3111	3009	3018	2707
2668	3036	2940	2997	3001	3010	1827
2648	2989	2894	1801	1904	1901	1690
1589	1503	1512	1527	1513	1514	1523
1577	1491	1495	1469	1499	1505	1503
1515	1479	1487	1462	1497	1499	1454
1484	1456	1481	1399	1484	1490	1449
1473	1428	1426	1323	1436	1441	1416
1410	1421	1424	1264	1418	1423	1283
1391	1230	1283	1199	1367	1361	1228
1370	1223	1254	1164	1209	1225	1205
1302	1143	1218	1135	1146	1168	1154
1207	1003	1001	991	1117	1116	1048
1117	923	985	857	960	1020	962
1065	879	950	720	954	953	923
913	742	819	663	901	914	823
883	726	764	570	848	841	611
878	693	684	491	482	472	537
766	479	465	434	417	371	430
513	470	401	388	370	354	415
385	196	232	291	284	222	344
319	172	180	137	218	172	293
196	129	114	119	174	165	182
171	69[b]	60[b]	24[b]	161	111	28[b,c]
129	52[b]			110		

[a] See Figure 1 for species. [b] These very low frequencies are uncertain because the geometry optimization used a different basis set than the force matrix calculations. Frequencies above 100 cm^{-1} are affected only slightly by this procedure. See text. [c] This 28 cm^{-1} mode was replaced by a 110 cm^{-1} mode in all calculations. See text.

TABLE 3: Selected Rotational Constants (cm^{-1}) Used in RRKM Calculations for $Ni^+ + C_3H_8$ Reaction[a]

1	2	TS_{CC}	$MCTS_{CH_4}$	4	TS_{CH} (2°)	$MCTS_{H_2}$ (2°)	$MCTS_{H_2}$ (1°)
0.275	0.376	0.251	0.380	0.241	0.239	0.252	0.345
0.120	0.105	0.152	0.111	0.121	0.122	0.145	0.093
0.088	0.086	0.102	0.096	0.090	0.091	0.103	0.081

[a] See Figures 1 and 3 for species.

ground state ($3d^9$,^2D) reactants, corrected for differential zero-point energy and for 3d orbital occupancy as described above. Results for both $Ni^+ + C_3H_8$ and $Ni^+ + C_3D_8$ are given. Harmonic vibrational frequencies and rotational constants at each stationary point (Tables 2 and 3) will be used directly in the statistical rate calculations.

In the statistical rate modeling, the energies of the multicenter transition states (MCTSs) will determine product branching fractions, since these are by far the highest potential energy points on each reaction path. The geometries of these key transition states are shown in Figure 3. The lowest of these barriers is $\mathbf{MCTS}_{CH_4}$ at +3.1 kcal/mol, which involves β-hydrogen migration following CC insertion. The next lower barrier is $\mathbf{MCTS}_{H_2}(\mathbf{2}°)$ at +5.0 kcal/mol, involving β-hydrogen migration following *secondary* CH insertion. Substantially higher is $\mathbf{MCTS}_{H_2}(\mathbf{1}°)$ at +11.4 kcal/mol, involving β-hydrogen migration following *primary* CH insertion. The kinetic modeling below indicates that the 6.4 kcal/mol difference between $\mathbf{MCTS}_{H_2}(\mathbf{2}°)$ and $\mathbf{MCTS}_{H_2}(\mathbf{1}°)$ is sufficiently large to render primary CH insertion unimportant at low collision energy. Significantly, B3LYP finds $\mathbf{MCTS}_{CH_4}(\mathbf{1}°)$, the TS involving *β-methyl* migration following initial primary CH insertion, to lie at +16.8 kcal/mol, far above the other route to CH_4 elimination via CC insertion. These MCTS energies lie in the same order found for $Fe^+ + C_3H_8$ by Holthausen and Koch.[14]

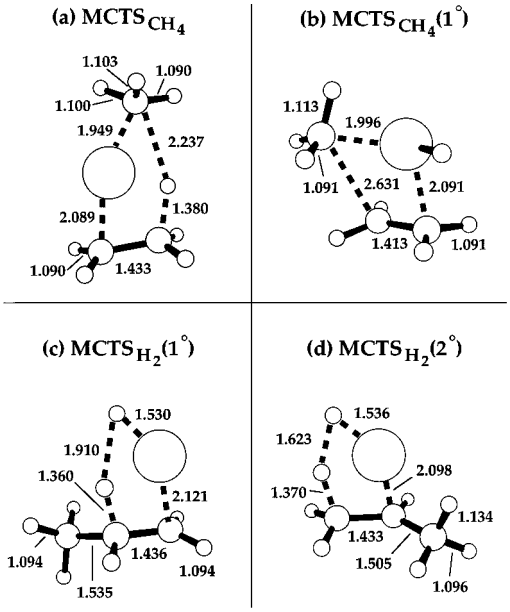

Figure 3. Optimized geometries of key multicenter transition states en route to (a) CH_4 elimination via initial CC insertion; (b) to CH_4 via initial primary CH insertion, (c) to H_2 elimination via initial primary CH insertion, and (d) to H_2 via initial secondary CH insertion.

Some tests were performed to investigate the reliability of the calculated potential surface. First, the geometry optimization of certain multicenter transition states was improved by using a larger basis set than the LANL2DZ basis decribed above. For nickel the contraction of the Wachters all-electron basis set invoked by using the 6-311+G keyword in Gaussian 94 was used, and for the other atoms polarization functions were added to the double-ζ basis. It was found that, for the geometries obtained using this basis, the relative energy calculated using the large 6-311+G(2d,2p) basis set decreased by less than 1 kcal/mol compared to the structures obtained in the original LANL2DZ optimization.

Second, PCI-X^2 calculations were performed for some of the stationary points. In the PCI-*X* scheme the calculated correlation effects on the relative energies are extrapolated using the empirically determined parameter *X*. For MCPF[31] calculations using double-ζ plus polarization basis sets the best value of the parameter *X* has been determined to be 80; i.e., 80% of the correlation effect is assumed to be obtained in the calculation.[2] For $\mathbf{MCTS}_{H_2}(\mathbf{2}°)$, the PCI-80 scheme gives a relative energy of 6.5 kcal/mol, indicating that the B3LYP value of 5.0 kcal/mol is reliable. The PCI-*X* method can only be used when the underlying correlation method, in this case MCPF, is valid. Unfortunately, for $\mathbf{MCTS}_{CH_4}$ the MCPF method breaks down due to large near-degeneracy effects. Thus, no comparison to PCI-*X* can be made for this TS. However, previous calculations on nickel-containing systems have shown that the B3LYP method can give reliable results even in situations where the PCI-80 scheme breaks down.[4b] To finally settle the question of the accuracy of the calculated barrier heights, much larger multireference calculations using large basis sets must be carried out. Such calculations are beyond the scope of the present study.

Finally, the calculated gas-phase exothermicity for the dominant elimination process $Ni^+ + C_3H_8 \rightarrow NiC_2H_4^+ + CH_4$ is 33.3 kcal/mol, compared with the best experimental estimate of 27.0 ± 1.2 kcal/mol.[32] The B3LYP exothermicity for Ni^+

$+ C_3H_8 \rightarrow NiC_3H_6^+ + H_2$ is 23.6 kcal/mol, compared with the experimental estimate of 17.3 ± 2.3 kcal/mol.

IV. Statistical Model for Decay of $Ni(C_3H_8)^+$ Complexes

The model for complex decay includes dissociation back to reactants (k_{diss}) and two parallel elimination paths (Figure 2): one involving CC insertion and subsequent CH_4 elimination (k_{CH_4}) and the other involving secondary CH insertion and subsequent H_2 elimination (k_{H_2}). Other paths lie at substantially higher energy and are assumed not to contribute at the low collision energies of greatest interest here. Each path includes multiple potential minima and transition states (TSs), all of whose energies and vibrational frequencies could affect the overall rate of fragmentation. The calculations assume an initial population of long-lived complexes with fixed total energy E but a distribution of angular momenta J determined by the Langevin cross section,[33] which scales with translational energy $E_t^{-1/2}$. That is, we assume $J = l$, where l is the initial orbital angular momentum of the collision. This neglects rotational angular momentum j of the propane reactant, a good approximation for our cold reactants.[8] We first calculate microcanonical forward and reverse unimolecular rates $k_i(E,J)$ for passage between successive minima in Figure 1. In calculating k_{diss}, we further assume that $l' = l$, i.e., that no angular momentum transfers into rotation of propane. We discuss this simplifying assumption below. The microcanonical rates are then combined in a parallel decay, steady-state approximation[34] to yield the overall decay rate of complexes $k_{tot}(E,J)$ and the time-dependent branching fractions among the three fragmentation channels, $Ni^+ + C_3H_8$, $NiC_2H_4^+ + CH_4$, and $NiC_3H_6^+ + H_2$.

A. Microcanonical Kinetics Model. To relate the microcanonical rate constants for individual reaction steps of Figure 1 to the observed macroscopic decay times, we postulate the kinetics scheme of Figure 2. Baer and co-workers have used a similar strategy to model complex unimolecular reactions.[35] The general solution of even this simplified scheme would involve multiexponential decay of the $Ni(C_3H_8)^+$ complexes, even for selected (E,J). However, the energetics gleaned from the electronic structure work place each elimination channel in a much simpler, *steady-state limit*. The overall decay of the complex for fixed (E,J) then becomes *exponential* with rate constant:

$$k_{tot}(E,J) = k_{diss}(E,J) + k_{CH_4}(E,J) + k_{H_2}(E,J) \qquad (2)$$

In eq 2, k_{diss} is the microcanonical rate constant for dissociation back to reactants. Each of the two elimination rates is obtained by applying the steady-state approximation to the appropriate short-lived intermediate, either the CC insertion intermediate **2** or the secondary CH insertion intermediate **4**. In terms of the microcanonical rates, the steady-state rates are given by

$$k_{CH_4}(E,J) = k_{CC}k_{MC}^{CH_4}/(k_{-CC} + k_{MC}^{CH_4}) \qquad (3)$$

and

$$k_{H_2}(E,J) = k_{CH}k_{MC}^{H_2}/(k_{-CH} + k_{MC}^{H_2}) \qquad (4)$$

Each of the microcanonical rates k_i on the right-hand sides of eqs 3 and 4 depends on (E,J) in a manner to be calculated by RRKM theory.

The justification for the steady-state expressions comes from the actual relative magnitudes of the microcanonical rates when the energetics are roughly constrained to conform with theory. Using the CH_4 channel as an example, the steady-state limit holds whenever $k_{CC} \ll (k_{-CC} + k_{MC}^{CH_4})$.[34] We will find that as long as the CC insertion intermediate **2** lies at least 10 kcal/mol above the complex **1**, k_{CC} will be slow compared with k_{-CC} because the vibration−rotation density of states at **1** far exceeds the density of states at **2**. For similar reasons, we can neglect the backward step from **3** to **2**. Complexes that reach **3** are far more likely to eliminate CH_4 by crossing the low-energy exit channel orbiting transition $\mathbf{TS_{orb}}'$ than to return to **2** over the much higher energy $\mathbf{MCTS}_{CH_4}$. Similar reasoning applies to the H_2 elimination channel at low J. For high J, a fraction of exit-channel complexes might return from **5** over the MCTS toward the complex **1**, reflected by a high centrifugal barrier to elimination of H_2. We discuss this minor effect in section V.D.

The parallel, exponential decay embodied in eq 2 assumes that all three decay channels share a common long-lived intermediate, which we describe somewhat simplistically as *the* ion−dipole complex **1**. Based on earlier electronic structure calculations,[14,36] there likely exist *several* local minima with Ni^+ bound to various "sites" on the propane molecule. It is plausible that *different* minima might be the direct precursors to CC insertion, primary CH insertion, and secondary CH insertion. The justification for lumping all such precursors together as one species in the kinetics scheme is that we expect all such wells to be very deep (≈30−35 kcal/mol) compared with the heights of the barriers between them (≤5 kcal/mol). In single-collision conditions, the high internal energy of collision complexes then allows Ni^+ to sample different local minima freely and rapidly. If interconversion of the different local minima is very fast on the time scale of both insertion and dissociation, then the entire collection of "equilibrated" ion−dipole complexes will behave as a single species in the overall kinetics scheme.

For comparison with the experimental results of paper 1, we must calculate the rate of production of each of the three products of $Ni(C_3H_8)^+$ complex decay as a function of E, J, and the time t. Within the steady-state, parallel decay approximations, each rate is given by

$$\frac{1}{[NiC_3H_8^+]_0}\frac{dn_i}{dt} = k_i(E,J)e^{-k_{tot}(E,J)t} \qquad (5)$$

where i stands for one of three channels, dissociation, H_2 elimination, or CH_4 elimination; n_i is the number density of product i; and $[Ni(C_3H_8)^+]_0$ is the density of complexes at $t = 0$.

The rate of association of Ni^+ with C_3H_8 is taken as the classical Langevin ion-induced dipole capture rate constant $k_L = \sigma_L v_{rel}$, where σ_L is the Langevin cross section. The relative velocity is related to the collision energy by $E_t = {}^1/_2\mu v_{rel}^2$. Assuming 6.3 Å^2 for the polarizability of C_3H_8,[37] σ_L increases from 50 Å^2 at 0.7 eV to 90 Å^2 at 0.21 eV to 420 Å^2 at 0.01 eV; k_L is 1.2×10^{-9} cm^3 s^{-1}, independent of E_t. Since our kinetics model begins with a population of $Ni(C_3H_8)^+$ at $t = 0$, k_L enters the modeling only by determining the distribution of orbital angular momenta l that contribute to the Langevin cross section.[33] We must average eq 5 over the probability distribution $P(J) = 2J/J_{max}^2$. Here J_{max} equals the largest l that can penetrate the orbiting transition state, as determined by the Langevin cross section. J_{max} scales as $E_t^{1/4}$; it is 367 at 0.7 eV, 272 at 0.21 eV, and 127 at 0.01 eV. For the two elimination channels, the centrifugal barrier atop some subsequent potential energy barrier further limits the range of J that can proceed to products, as described below.

TABLE 4: $NiC_3H_8^+$ Energetics for Models 1−3

species[b]	model 1[c]	model 2[d]	model 3[e]
complex **1**	−36	−39.3, −28.5[f]	−39.3, −28.5[f]
$\mathbf{TS}_{CC}$	−11	−10.0	−2.3
$Ni(CH_3)(C_2H_5)^+$	−19	−17.0	−17.0
$\mathbf{MCTS}_{CH_4}$	+3.1	−2.5	−12.0
$\mathbf{TS}_{CH}(\mathbf{2}°)$	−11	−11.0	−0.9
$Ni(H)(iso\text{-}C_3H_7)^+$	−12	−12.0	−12.0
$\mathbf{MCTS}_{H_2}(\mathbf{2}°)$	+5.0	−2.2	−10.0

[a] Energies in kcal/mol relative to reactants, including ΔZPE_H corrections appropriate to $Ni^+ + C_3H_8$. [b] See Figure 1. [c] From density functional theory (Table 1). [d] Preferred model; see text. [e] Successful model that places insertion TSs *above* multicenter TSs. [f] Two entries illustrate the range of energies for the complex **1** that can produce complex decay time scales that match experiment, depending on the model used for internal rotational motions. See text.

The *J*-averaged result takes the form

$$\frac{1}{[NiC_3H_8^+]_0}\left\langle\frac{dn_i}{dt}\right\rangle_J = \sum_{J=0}^{J_{max}} P(J)\, k_i(E,J) e^{-k_{tot}(E,J)t} \qquad (6)$$

It remains to integrate this rate expression over the appropriate range of time to obtain the total density of products formed during a time window chosen to match a particular experimental measurement. We must also average that result over the uniform distribution of *collision initiation times*, as determined by the ion extraction time t_{ext} discussed in section II.A of paper 1. The resulting time-dependent decay probabilities and branching fractions for a particular model can then be compared directly with experiment.

B. Details of RRKM Rate Calculations. All energies are given relative to ground-state reactants, $Ni^+(3d^9,{}^2D_{5/2}) + C_3H_8$. Differential zero-point-energy corrections for each of the isotopomers C_3H_8, $CH_3CD_2CH_3$, $CD_3CH_2CD_3$, and C_3D_8 are calculated from the B3LYP harmonic frequencies and included in all the energies discussed below. The set of initial energetic estimates taken directly from theory is called model 1 in Table 4. B3LYP finds the $Ni^+(C_3H_8)$ complex **1** to lie at −35.6 kcal/mol. For comparison, the same level of theory finds the $Ni^+(C_2H_6)$ and $Ni^+(C_4H_{10})$ complexes analogous to **1** at −22 and −37 kcal/mol relative to the respective Ni^+ + alkane asymptotes. For the energies of **2**, $\mathbf{TS}_{CC}$, **3**, **4**, $\mathbf{TS}_{CH}$ **(2°)**, and **5**, we use the results directly from B3LYP theory (model 1). The results are insensitive to these energies. The energies of $\mathbf{MCTS}_{CH_4}$ and $\mathbf{MCTS}_{H_2}(\mathbf{2}°)$, which will prove critical in determining product branching fractions, are treated as mildly adjustable parameters.

To calculate each of the microcanonical rates $k_i(E,J)$ in Figure 3, we use the statistical rate theory known as RRKM theory.[19−21] In doing so, we implicitly assume that reaction occurs on a single potential energy surface, that intramolecular energy redistribution is instantaneous on the time scale of each reaction step, and that, in the language of classical mechanics, there are no "recrossing" trajectories that pass forward and then backward across the transition state. Under these assumptions, each microcanonical unimolecular rate constant is given by

$$k_i(E,J) = n_i \frac{W_i^\dagger(E - E_0 - E_r^\dagger(J))}{h\rho_i(E - E_r(J))} \qquad (7)$$

where n_i is the reaction path degeneracy, $W_i^\dagger$ is the sum of vibration−rotation states at the transition state, and ρ_i is the density of vibration−rotation states for the reactant. The Beyer−Swinehart direct-count algorithm[20,21,38] is used to evaluate the density and sum of states. In our calculations, we define E as the total reactant energy above the zero-point energy of the $Ni(C_3H_8)^+$ complex, including collision energy E_t, any electronic energy of Ni^+, and any internal energy of C_3H_8. E_0 is the activation energy (bare potential energy surface barrier height corrected for zero-point-energy differences between TS and reactant, Table 4). $E_r(J)$ and $E_r^\dagger(J)$ are "inactive" rotational energies of the reactant and the transition state *unavailable* for passage over the barrier. The amount of energy tied up in overall rotation of the complex changes as the reaction proceeds because the moments of inertia change. In modeling our own molecular beam experiments in which C_3H_8 is internally cooled, we add no internal energy to reactants beyond that carried by E_t. In modeling Armentrout's ion beam experiments with C_3H_8 at 300 K, we add 1 kcal/mol extra internal energy.

The 12-atom Ni^+/C_3H_8 system has 36 degrees of freedom; three are translation of the center of mass, and three more are *external* rotations about the three principal inertial axes. For reactants $Ni^+ + C_3H_8$, the 30 *internal* degrees of freedom include three for relative translation and the 27 vibrations of bare C_3H_8. On formation of the $Ni(C_3H_8)^+$ complex, the three relative translations become three (soft) vibrations. In the simplest view, these are one stretching vibration and two bending vibrations. Most of the choices encountered in modeling the rates involve the treatment of these two "soft bends" of the complex and the torsional modes of the methyl groups, which number either one or two at different stages of the reaction. At $\mathbf{TS}_{orb}$ and in the complex **1**, we explored the effects of treating the soft bends either as harmonic vibrations or as a two-dimensional free internal rotor. We also explored the effects of treating the methyl rotors at various stationary points as free or harmonic. These efforts are discussed in detail below.

It is very important to capture the most important effects of angular momentum conservation. Our treatment is simple. We approximate the total angular momentum J of the complex as equal to the orbital angular momentum l brought to the complex by the ion−molecule collision, which is appropriate for the internally cold reactants of paper 1. For all wells and transition states, the complex is approximated as a prolate symmetric top with principal moments of inertia I_a, I_b, and I_c, where $I_a \ll I_b \approx I_c$. The corresponding rotational constants are A, B, and C. The line of approach is taken as the a axis. As the collision proceeds, the orbital angular momentum J evolves into the two external rotations of the complex about the b and c axes, perpendicular to the line of approach. The rotational energy levels for the approximate symmetric top rigid rotor are given by

$$E_r(J) = \left(\frac{1}{I_b} + \frac{1}{I_c}\right)\frac{J(J+1)\hbar^2}{4} \qquad (8)$$

The third external rotation about the line of approach is assumed to be active for both the reactant and the transition state and is included in the state densities. That is, we assume that K is not conserved on the nanoseconds−microseconds time scale of our reaction. The classical expression

$$\rho(E) = (AE)^{-1/2} \qquad (9)$$

is used for this one-dimensional rotational density of states.

A priori modeling of the density of states for the complex **1** and for the orbiting transition state $\mathbf{TS}_{orb}$ deserves special comment. This is difficult primarily due to the soft degrees of freedom. In the complex, these include the $Ni^+-C_3H_8$ stretch,

the two soft bends, and two methyl torsions. The actual $Ni^+-C_3H_8$ potential is likely very flat, with multiple shallow minima at about −35 kcal/mol separated by low barriers whose heights are perhaps 5 kcal/mol or less. Since the internal energy of the complex far exceeds these barriers to internal motion, the harmonic approximation surely underestimates the density of states from the soft motions. In modeling **1**, we view the harmonic approximation as one extreme limit providing a lower bound on the rovibrational density of states. A second extreme limit is *free internal rotation*, which likely provides an upper bound on the density of states. This limit is quite appropriate for methyl internal rotations in the complex **1**, for which the average energy in these modes far exceeds the typical barrier height of 3 kcal/mol. At sufficiently high internal energy, the two soft bends might *also* be better modeled as two-dimensional free internal rotation of C_3H_8 relative to Ni^+, much as in $\mathbf{TS_{orb}}$ but with different moments of inertia. The density of states for such a two-dimensional rotor is

$$\rho(E) = \bar{B}^{-1} \tag{10}$$

where we take $\bar{B}$ as the geometric mean of the reduced moments of inertia about the two axes perpendicular to the approach axis. Approximate expressions for these reduced moments of inertia are given in ref 39. For example, for $J = 100$, the distance between Ni^+ and the center of mass of C_3H_8 decreases from about 10 Å at $\mathbf{TS_{orb}}$ to about 2.3 Å in the complex **1**, so that $\bar{B}$ increases from 0.488 cm^{-1} at $\mathbf{TS_{orb}}$ to 0.636 cm^{-1} in **1**. We will explore different treatments of **1** in combination with different assumed well depths in an effort to match the absolute experimental time scale of the complex decay. When a harmonic vibration is replaced by free internal rotation, the corresponding density of states is convolved with the remaining vibrational contributions to the density of states, as described in detail by Gilbert and Smith.[20]

Modeling of the orbiting transition state $\mathbf{TS_{orb}}$ involved in k_{diss} requires still further choices. We assume that the distribution of orbital angular momentum l at $\mathbf{TS_{orb}}$ is the same as the distribution brought to the complexes by the original Langevin collisions, i.e., that no net angular momentum is transferred to $\boldsymbol{j}$, rotation of the propane molecule, during a collision that evolves (slowly) back to $Ni^+ + C_3H_8$. This fairly standard assumption simplifies the calculations. Phase space theory would make the alternative hypothesis of randomization of the distribution of total angular momentum $\boldsymbol{J} = \boldsymbol{l} + \boldsymbol{j}$ between orbital angular momentum $\boldsymbol{l}$ and propane rotation $\boldsymbol{j}$. We comment on the effects of this assumption later in Secs. V−D and VI-D. For each (E,J), the distance R_{TS} between Ni^+ and the C_3H_8 center of mass at the orbiting TS is then taken as the maximum of the sum of the ion-induced-dipole attractive potential plus the centrifugal potential $\hbar^2 J(J+1)/2\mu R^2$, where μ is the reduced mass of the Ni^+/C_3H_8 collision pair. This is a kind of variational transition state theory. The actual values of R_{TS} are quite large. For example, at $E_t = 0.21$ eV, $R_{TS} = 10$ Å for $J = 100$ and 5 Å for $J = 200$. The internal degrees of freedom of $\mathbf{TS_{orb}}$ include the reaction coordinate R; three external rotations, two of whose moments of inertia depend on J via R_{TS}, and 29 vibrations. The two soft bends of the $Ni(C_3H_8)^+$ complex presumably become even softer at the orbiting TS. They are modeled either as lower frequency harmonic vibrations or as a two-dimensional free internal rotation due to the magnitude of R_{TS}. Both of the methyl internal rotors of propane survive at $\mathbf{TS_{orb}}$. In contrast to the $Ni(C_3H_8)^+$ complex, which is internally very hot, the orbiting TS has very little internal energy, so we treat the methyl rotors at $\mathbf{TS_{orb}}$ as harmonic vibrations.

The B3LYP calculations found one unusually low vibrational frequency of 28 cm^{-1} for $\mathbf{MCTS}_{H_2}(\mathbf{2°})$. This is a complicated mode; it is not internal methyl rotation. As discussed in section III, frequencies below about 100 cm^{-1} are unreliable. We tested the effect of replacing the 28 cm^{-1} mode with a 110 cm^{-1} mode. This substitution has no effect on the overall reaction efficiency because H_2 elimination is such a minor product. However, use of the 110 cm^{-1} mode decreases the density of states at $\mathbf{MCTS}_{H_2}(\mathbf{2°})$ moderately, which in turn causes us to *lower* our estimate of the energy of this barrier by about 1 kcal/mol in order to recover the proper H_2/CH_4 branching ratio. We kept the 110 cm^{-1} mode in all subsequent calculations, primarily because it allows us to reproduce the experimental H_2:CH_4 branching ratio vs E_t much better than the 28 cm^{-1} mode.

We must also incorporate symmetry effects into the microscopic rates by calculating the reaction path degeneracy.[19−21,40] Following Pechukas[40] and the illustrations in the book by Gilbert and Smith,[20] we first evaluate microscopic rates from eq 7 without the use of any symmetry numbers. The microscopic rates must then be multiplied by the *reaction path degeneracy*:

$$n = m^\dagger \sigma / m \sigma^\dagger \tag{11}$$

where m and $m^\dagger$ are the number of optical isomers of the reactant and transition state, respectively, and σ and $\sigma^\dagger$ are the corresponding "symmetry numbers". For example, in calculating k_{diss}, the reactant is the $Ni(C_3H_8)^+$ complex **1** and the transition state is $\mathbf{TS_{orb}}$. For simplicity in counting, we choose a complex geometry and dissociation path that has C_{2v} symmetry about the approach axis R. Then $m = m^\dagger = 1$ (no optical isomers). For three carbons and eight hydrogens, there exist $3!8! = 24\,192$ equivalent conformations of both the reactant and TS. The symmetry numbers σ and $\sigma^\dagger$ give the number of equivalent conformations that can freely interconvert by overall rotation or internal rotation on the relevant experimental time scale. This depends on the modeling of soft motions. Each external rotation that interchanges equivalent nuclei brings a factor of 2 to σ; each methyl torsion treated as a free rotor brings a factor of 3; a methyl torsion treated as a triply degenerate vibration does not alter σ.

In the $Ni(C_3H_8)^+$ complex, suppose we treat both methyl groups as free rotors and the two soft bends as harmonic oscillators. Then $\sigma = 3 \times 3 \times 2 = 18$; the factor of 2 comes from external rotation about the approach axis. In the loose transition state $\mathbf{TS_{orb}}$, both methyls are treated as vibrations so that $\sigma^\dagger = 2$. The microscopic rate k_{diss} calculated from eq 7 using state densities *without* symmetry numbers must then be multiplied by a factor of *9* to take this change in conformational rigidity properly into account. In our final model, all methyl torsions are treated as free rotations except for two methyl torsions at $\mathbf{TS_{orb}}$. The resulting symmetry numbers for the different microscopic rates of Figure 2 are 2 for k_{CC}, 1 for k_{-CC}, 3 for $k4^{CH}_{MC}$, 2 for k_{CH}, 1 for k_{-CH}, and 3 for $k2^{H}_{MC}$. We include no explicit effects of optical isomerism even in the chiral MCTSs, because mirror images, when they occur, are very likely separated by a low-energy barrier to inversion, which then occurs rapidly on the nanoseconds−microseconds time scale of complex decay.

Finally, we must consider electronic degeneracy.[41] The $Ni^+(^2D_{5/2}) + C_3H_8$ reactants are 6-fold degenerate. Complexation of Ni^+ to propane lowers the symmetry and may split the spatial degeneracy into as many as three nondegenerate electronic states, each of doublet spin. Proper treatment of this electronic degeneracy along each reaction path would require knowledge of the excited-state potential energy surfaces. Lack-

ing such information, we assume no effects of electronic degeneracy on the calculated rates. In one limiting case, the three states are nearly degenerate in all configurations of interest, and a factor of 6 would appear in both the numerator and denominator of eq 7 and cancel. In the opposite extreme, one state might be much lower than the others for reactants while all three states are degenerate at the transition state, as might occur for k_{diss}. Then the rate calculated from eq 7 will be too low by a factor of 3.

In an attempt to learn how sensitive our energetic inferences are to the many choices inherent in the statistical modeling, we have expended much effort exploring the range of models consistent with a large set of experimental data. We will see that the wide variety of plausible treatments of $\mathbf{TS_{orb}}$ and of the complex **1** allows a wide compensating range of well depths of complex **1** (28.5−39.3 kcal/mol) to achieve agreement with the absolute experimental time scale of complex decay. The properties of several TSs and short-lived intermediates such as $\mathbf{TS_{CC}}$, $\mathbf{TS_{CH}(2°)}$, **2**, and **3** drop out entirely due to the applicability of the steady-state approximation. Fortunately, model predictions of the absolute cross section for CH_4 and H_2 elimination and of the CH_4 branching fraction are quite sensitive to the energies of $\mathbf{MCTS}_{CH_4}$ and $\mathbf{MCTS}_{H_2}(\mathbf{2°})$, rather independent of the other parameters in the model. For k_{diss}, the assumption of no angular momentum exchange between $\boldsymbol{l}$ and $\boldsymbol{j}$ primarily affects the modeling of **1** and of $\mathbf{TS_{orb}}$, which are tuned to fit the experimental time scale. An alternative is phase space theory, which assumes complete randomization of $\boldsymbol{l}$ and $\boldsymbol{j}$ subject to conservation of total angular momentum. A model using phase space theory might change the well depth of **1** somewhat, but the locations of $\mathbf{MCTS}_{CH_4}$ and $\mathbf{MCTS}_{H_2}(\mathbf{2°})$ would not be greatly affected. Overall, we estimate that all statistical models that fit the experimental data would place these key TSs within ±2 kcal/mol of the results of our preferred model 2 presented below.

V. Results and Comparison with Experiments

Our goal is to explore what range of models can reproduce four key sets of experimental data: the distribution of absolute time scales of $Ni(C_3H_8)^+$ complex decay at $E_t = 0.21$ eV, as described in paper 1;[8] the H_2 and CH_4 elimination cross section data $\sigma(E_t)$ from the Armentrout group;[11] the branching of the complex decay among the three fragment channels, $Ni^+ + C_3H_8$, $NiC_2H_4^+ + CH_4$, and $NiC_3H_6^+ + H_2$ in paper 1; and the deuterium isotope effect in changing from C_3H_8 to $CH_3CD_2CH_3$ to $CD_3CH_2CD_3$ to C_3D_8.[11] Fortunately, it quickly becomes clear how to adjust the model to vary the time scale, the absolute cross section, and the branching fractions roughly independently. This allows us to focus on a small subset of "model space". In the following description, all energies include differential zero-point corrections ΔZPE, as in Table 1.

A. Adjustment of Model Parameters. Using the B3LYP energetics labeled model 1 in Table 4 without adjustment predicts only 0.012% CH_4 elimination and no H_2 elimination at $E_t = 0.21$ eV, in sharp contrast with experiment. The reason is that the long-lived complex **1** is able to pass over the low barriers to insertion in CH and CC bonds, but the much higher multicenter transition states cause bottlenecks. Passage over these MCTSs is much too slow to compete with dissociation back to $Ni^+ + C_3H_8$ over the loose $\mathbf{TS_{orb}}$, so k_{diss} completely dominates k_{H_2} and k_{CH_4}. To fit Armentrout's absolute cross section for CH_4 elimination, it is necessary to lower $\mathbf{MCTS}_{CH_4}$ by 5.6 kcal/mol from the B3LYP value of +3.1 kcal/mol to a value near −2.5 kcal/mol, as in model 2 (Table 4). To fit the robust 4:1 CH_4:H_2 elimination branching ratio found in so many experiments, we must then also lower $\mathbf{MCTS}_{H_2}(\mathbf{2°})$ by about 7 kcal/mol compared with B3LYP. Its energy in model 2 becomes −2.2 kcal/mol, essentially identical with $\mathbf{MCTS}_{CH_4}$. If we lower $\mathbf{MCTS}_{H_2}(\mathbf{2°})$ by only 5.6 kcal/mol so that the energy *difference* between the two MCTSs remains the same as given by B3LYP, then the CH_4:H_2 branching ratio increases to 23:1, far in excess of the experimental value of 4:1. If we assume that all J's that cross $\mathbf{MCTS}_{H_2}(\mathbf{2°})$ make H_2 (no exit-channel effects), we can raise $\mathbf{MCTS}_{H_2}(\mathbf{2°})$ by only 0.6 kcal/mol. This is true even when we apply an approximate correction for tunneling through the centrifugal barrier atop the exit-channel orbiting TS, as described in section D.

Experiment shows that a majority of the complexes **1** revert to $Ni^+ + C_3H_8$ reactants and that substantial decay occurs on a 100 ns−20 μs time scale for $E_t = 0.21$ eV. This constrains the *combined* modeling of $\mathbf{TS_{orb}}$ and of the complex **1**, which together determine k_{diss} and thus the absolute time scale of complex decay. If we use the B3LYP estimate of −36 kcal/mol for the complex, treat methyl rotors as harmonic vibrations in **1** and in $\mathbf{TS_{orb}}$, and treat the two soft bending motions as free internal rotation in $\mathbf{TS_{orb}}$ but as harmonic vibrations in **1**, then we find k_{diss} on the order of 10^7 s^{-1} at $E_t = 0.21$ eV, which is about 2 orders of magnitude too fast. Such a "loose" model for $\mathbf{TS_{orb}}$ seems physically reasonable, so it is necessary to increase the density of states of **1**. Fortunately, this does not alter the branching among Ni^+, $NiC_2H_4^+$, and $NiC_3H_6^+$, since to a good approximation $\rho(\mathbf{1})$ enters the denominator of all three rates in eq 2, as we show below. We can increase $\rho(\mathbf{1})$ by orders of magnitude by increasing the binding energy of **1**, by converting methyl rotors from harmonic vibrations to free internal rotation, by converting the two soft bending motions from harmonic vibrations to free internal rotations, or by different combinations of two or three of these adjustments. In practice, we always modeled the two methyl rotors as free internal rotations, since this is physically reasonable at the large internal energy of **1**. After properly accounting for symmetry numbers, this increases $\rho(\mathbf{1})$ by a factor of 6 at $E_t = 0.21$ eV.

The dual entry for the energy of **1** under model 2 in Table 4, −39.3 and −28.5 kcal/mol, shows two very different values which can bring k_{diss} into the range of experiment. If the soft bends are harmonic with frequencies 129 and 171 cm^{-1} from the B3LYP frequencies of Table 2, then the binding energy of the complex must be increased to 39.3 kcal/mol to achieve large enough $\rho(\mathbf{1})$. Alternatively, if the bending motions of **1** are taken as two-dimensional free internal rotation of C_3H_8 relative to Ni^+ with density of states given by eq 10, then the binding energy must be decreased to 28.5 kcal/mol. These two binding energies should roughly bracket the physically reasonable limits. Evidently, we cannot determine the binding energy of **1** very accurately from our lifetime data. The smaller binding energy of 28.5 kcal/mol is in good agreement with the estimate of 30.9 kcal/mol for the $Co^+-C_3H_8$ binding energy from the threshold collision activation study.[42] However, interpretation of those experiments is presumably sensitive to the same modeling issues we confront here.

With the adjustments embodied in model 2, both the product branching and the absolute time scale of the decay can be brought into reasonable agreement with experiment, as described in detail below. It then becomes clear that the steady-state approximation embodied in the parallel kinetics model of eqs 2−4 is numerically valid for model 2, and indeed for all models reasonably similar to that predicted by B3LYP. The approximation holds as long as the CC and CH insertion

intermediates **2** and **4** both lie at least 10 kcal/mol above the complex **1**. The electronic structure calculations firmly support this limit. When steady state holds, both k_{CH_4} and k_{H_2} become *independent* of the well depths of the corresponding insertion intermediates, **2** and **4**. This is easily seen by writing out the appropriate expression for each k_i in eq 2. For the CH_4 channel the result is

$$k_{CH_4} = \frac{W^\dagger(\mathbf{TS}_{CC})\, W^\dagger(\mathbf{MCTS}_{CH_4})}{h\rho(\mathbf{1})(W^\dagger(\mathbf{TS}_{CC}) + W^\dagger(\mathbf{MCTS}_{CH_4}))} \qquad (12)$$

The steady-state limit thus places a factor of $\rho(\mathbf{1})$ in the denominator of k_{CH_4} and k_{H_2} in addition to k_{diss}. This explains why the absolute time scale of the complex decay decouples from the product branching fractions as described above. The density of states of the CC insertion intermediate has dropped out of the expression. An analogous expression holds for k_{H_2} in the steady-state limit.

If, in addition, $\mathbf{MCTS}_{CH_4}$ lies well above $\mathbf{TS_{CC}}$ as the calculations indicate, then we have not only $k_{-CC} + k_{MC}^{CH_4} \gg k_{CC}$ (the steady-state limit)[34] but also $k_{-CC} \gg k_{MC}^{CH_4}$. In that case, $W^\dagger(\mathbf{TS_{CC}}) \gg W^\dagger(\mathbf{MCTS}_{CH_4})$, and the expression further simplifies to

$$k_{CH_4} = W^\dagger(\mathbf{MCTS}_{CH_4})/h\rho(1) \qquad (13)$$

An analogous expression holds for k_{H_2}. This expression is like an RRKM rate constant for a single step in which the complex **1** reacts by crossing $\mathbf{MCTS}_{CH_4}$ directly without intervening steps. The reason is that the shallow $CH_3{-}Ni^+{-}C_2H_5$ well has negligible impact on the rate.

To illustrate that a variety of energetic models can fit the elimination branching ratios, we also explored models that place $\mathbf{TS_{CC}}$ and $\mathbf{TS_{CH}}$ *above* the multicenter TSs. One example is model 3 in Table 4, which essentially inverts the roles of the two types of TS in both the CH_4 and the H_2 channels. In this case, the sum of states at $\mathbf{TS_{CC}}$ and at $\mathbf{TS_{CH}}$ controls the elimination branching. The results now become quite insensitive to the exact placement of $\mathbf{MCTS}_{CH_4}$ and $\mathbf{MCTS}_{H_2}$, as long as each lies well below its respective bond insertion TS. Experiment cannot distinguish between model 2 and model 3, but the B3LYP calculations fall in much better agreement with model 2, which we therefore prefer.

B. Cross Sections and Time-Dependent Branching Fractions from Model 2. In Figure 4a, we compare the predictions of model 2 with the experimental elimination cross-section data (sum of CH_4 and H_2) of Armentrout and co-workers.[11] The model overestimates the cross section by about 30% at 0.05 eV, but it recovers the shape of the cross section curve quite well from 0.05 to 1 eV. Beyond that the data fall off abruptly, but the model results do not. This could be due to the onset of an endothermic fragmentation channel missing from the model. The model finds increasing CH_4 branching fraction with collision energy, in qualitative agreement with experiment (Figure 4b). As E_t increases, a larger and larger fraction of the possible contributions to k_{H_2} are cut off by orbital angular momentum effects.

Next we examine the detailed time evolution of complexes into the three fragmentation channels as predicted by model 2. At $E_t = 0.21$ eV, Figure 5a,b shows the J dependence of the microcanonical rates $k_i(E,J)$ that enter the steady-state expressions for k_{H_2} and k_{CH_4} (eqs 3 and 4). In the CH_4 elimination channel, we see that CC bond insertion (k_{CC}) is much slower

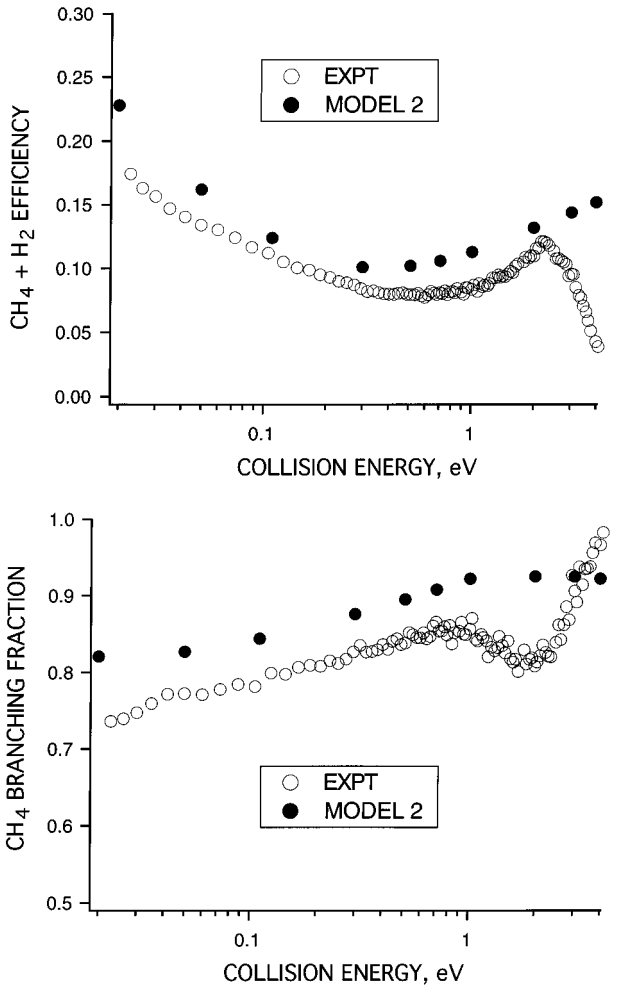

Figure 4. (a) Comparison of predictions of model 2 (solid dots) with the experimental elimination cross section data (sum of CH_4 and H_2) of Armentrout and co-workers (open circles, ref 11). (b) Fraction of elimination products branching to CH_4 from model 2 (solid dots) and from experiment (open circles, courtesy of P. B. Armentrout, unpublished data).

than its reverse (k_{-CC}). That is because the density of states of the deep $Ni(C_3H_8)^+$ complex well is so large. All three rates k_{CC}, k_{-CC}, and $k_{MC}^{CH_4}$ *decrease* as J increases. The cutoffs at high J arise from the differential effects of the centrifugal potential; this is purely a *mass distribution effect*. As reactants move from complex to CC insertion intermediate to $\mathbf{MCTS}_{CH_4}$, the moments of inertia *decrease*; i.e., mass is drawn toward the center of mass as the entire system becomes more compact in space. Thus, the centrifugal potential at $\mathbf{TS_{CC}}$ cuts off k_{CC} and k_{-CC} near $J = 200$. The centrifugal potential at $\mathbf{MCTS}_{CH_4}$ cuts off $k_{MC}^{CH_4}$ near $J = 160$, which sets the limit on the range of J that contributes to the $NiC_2H_4^+ + CH_4$ products. Using the estimated exothermicity of 25.6 kcal/mol for CH_4 elimination[32] and assuming that *all* orbital angular momentum brought to the complex becomes orbital angular momentum in products, the exit-channel $\mathbf{TS_{orb}}'$ sets the limit $J \leq 253$. Figure 5a shows why the steady-state limit of eqs 2−4 holds for all J at 0.21 eV and also why k_{CH_4} approaches the simple ratio of eq 3.

Analogous effects occur in the H_2 elimination channel (Figure 5b). The high-J cutoffs are somewhat different. However, due to the small reduced mass of $NiC_3H_6^+ + H_2$ product and the low polarizability of H_2, the high-J cutoff for overall H_2 elimination might now occur not at $\mathbf{MCTS}_{H_2}$, but at $\mathbf{TS_{orb}}''$, as earlier suggested by Bowers and co-workers.[10,11] For $E_t = 0.21$ eV complexes with $J \leq 141$ can cross $\mathbf{MCTS}_{H_2}$. Assuming

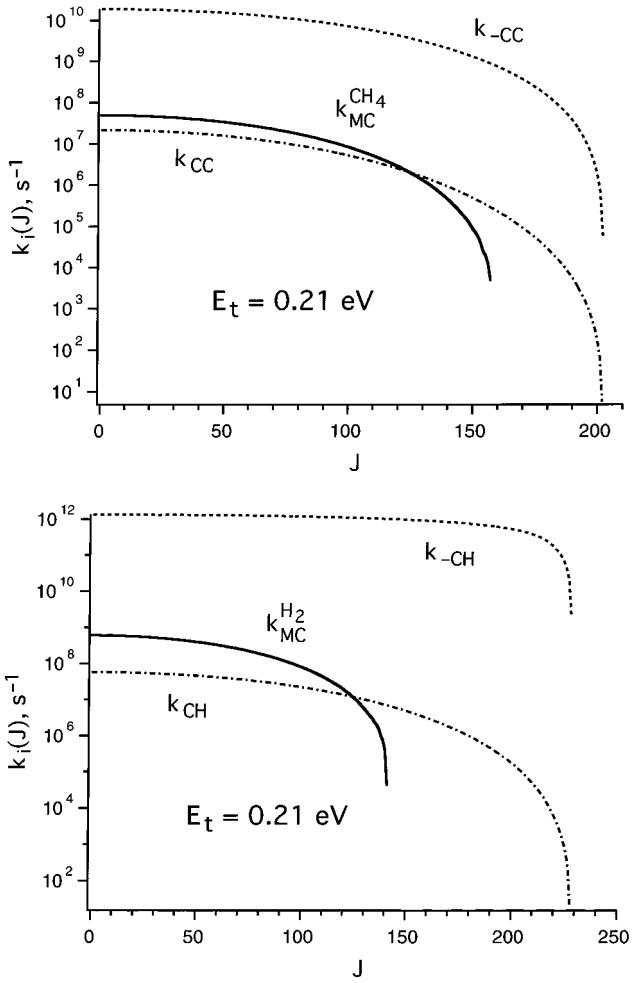

Figure 5. *J* dependence of microcanonical rates calculated from model 2 at $E_t = 0.21$ eV: (a) CH_4 elimination path; (b) H_2 path. See Figure 2 for definitions of individual rate constants.

the estimate of 15 kcal/mol for the exothermicity[32] and conservation of orbital angular momentum between entrance and exit, $\mathbf{TS_{orb}''}$ would set a more stringent cutoff at $J \leq 65$. Our elimination branching calculations assume the more stringent cutoff, but this is a small effect since k_{diss} dominates at high *J*.

The *J* dependence of k_{diss} (Figure 6) is opposite that of the elimination steps; i.e., $k_{diss}(E,J)$ *increases* with increasing *J*. As $Ni(C_3H_8)^+$ dissociates to $Ni^+ + C_3H_8$, mass moves *away from* the center of mass, raising the moment of inertia and decreasing the centrifugal potential at $\mathbf{TS_{orb}}$ compared with the complex **1**. Once again, we have assumed that the *J* distribution of dissociating complexes matches the distribution of complexes formed by Langevin collisions; i.e., no angular momentum is transferred to rotation of propane. The range of *J* that contributes to k_{diss} is then $J \leq 272$.

In Figure 6, we compare the *J* dependence of the three parallel decay rates k_{diss}, k_{CH_4}, and k_{H_2}. These are summed to form the overall complex decay rate $k_{tot}(E,J)$. For k_{H_2} the dotted portion of the curve represents the collision complexes that cannot eliminate H_2 due to the angular momentum constraints in the exit channel. We can see at a glance that elimination of CH_4 and of H_2 occurs primarily from complexes formed at low *J* (low impact parameter). While k_{CH_4} and k_{H_2} vary tremendously with *J* and k_{diss} varies over about 2 decades, their sum k_{tot} varies over less than 1 order of magnitude, from 10^5 to 10^6 s^{-1}.

Figure 7 shows a histogram of the distribution of k_{tot}, with the contribution from each *J* properly weighted by its probability

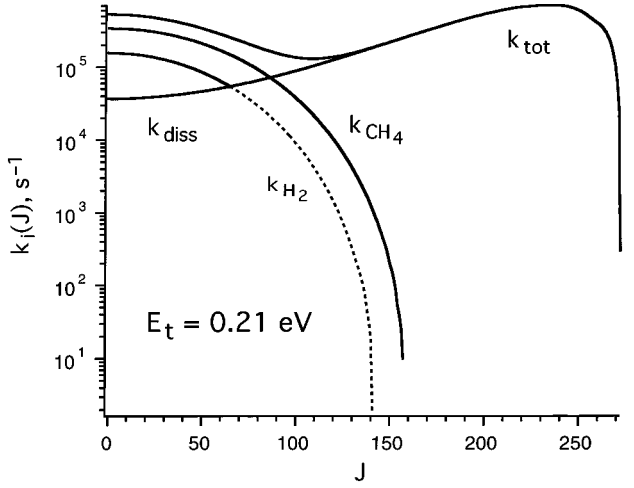

Figure 6. *J* dependence of k_{diss} and of the composite rates k_{CH_4} and k_{H_2} from eq 2 and model 2 at $E_t = 0.21$ eV. Total decay rate k_{tot} is the sum of the three parallel rates. Dashed line is continuation of H_2 curve beyond the limit $J \leq 65$ that would be imposed if all *J* of the complex became orbital angular momentum at $\mathbf{TS_{orb}''}$.

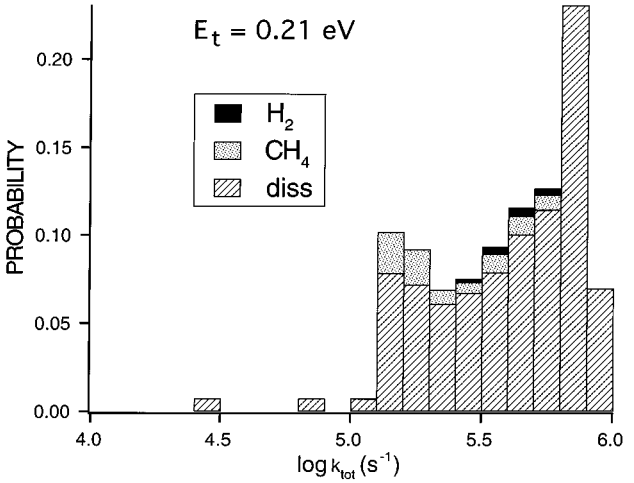

Figure 7. Histogram of the distribution of k_{tot}, with the contribution from each *J* weighted by $P(J) = 2J/J_{max}^2$. Each bar is partitioned according to the branching into the three decay channels.

density $P(J) = 2J/J_{max}^2$. Each bar is partitioned according to the branching into the three decay channels. The elimination products arise in roughly equal measure from all parts of the rate distribution. Even at $E_t = 0.21$ eV, the CH_4 elimination channel remains quite *inefficient*, although reactants have total energy 7.0 kcal/mol in excess of $\mathbf{MCTS}_{CH_4}$.

Finally, direct comparison with the time-resolved experiments of paper 1 requires proper weighting of each $k_{tot}(E,J)$ and calculation of the detailed rate of production of each decay channel as a function of time, as described in eq 6. Such a plot for model 2 is shown in Figure 8. The envelope of the three shaded areas gives the instantaneous total decay rate (number density/second) normalized to the initial complex density. The shaded areas partition the total rate into the contributions to each of the three product channels. The overall decay of the complex is *roughly* exponential, as the fairly narrow distribution of k_{tot} would suggest, but there is a significant tail at long times. Return of complexes to Ni^+ reactants dominates the branching on all time scales. The instantaneous ratio of rates for Ni^+ formation to CH_4 formation decreases substantially from 18:1 at $t = 0$ to 5:1 at $t = 20$ μs. The ratio of CH_4 to H_2 production varies even more, from 4:1 at $t = 0$ to 67:1 at $t = 20$ μs, perhaps explaining why we were unable to detect any

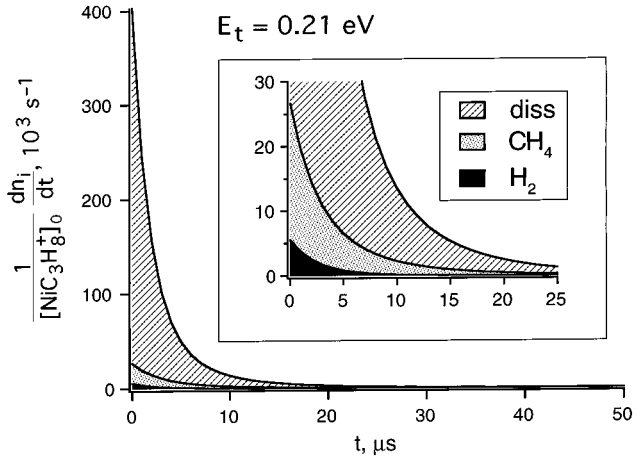

Figure 8. Instantaneous rate of formation of the three decay channels from model 2 at $E_t = 0.21$ eV. The shaded areas partition the total rate into the contributions to each of the three product channels as indicated.

TABLE 5: Branching Ratios vs Experiment, $t = 2-10$ μs after Collision[a]

	E_t (eV)	$NiC_2H_4^+ + CH_4$	$NiC_3H_6^+ + H_2$	$NiC_3H_8^+$
expt[a]	0.21	23 ± 4	4 ± 2	73 ± 4
model **2**[b]	0.21	21	4	75
model **3**[b]	0.21	21	4	75
expt[a]	0.01	3 ± 1	0.7 ± 0.4	96 ± 1
model **2**[b]	0.01	2.2	0.8	97

[a] Accompanying paper 1 (ref 8). Expt averages over this time interval in the kinetics models. [b] See Table 4 and text.

TABLE 6: $NiC_3H_8^+$ Fragmentation Pattern vs Experiment, $t = 16-24$ μs after Collision[a]

	E_t (eV)	$Ni^+ + C_3H_8$	$NiC_2H_4^+ + CH_4$	$NiC_3H_6^+ + H_2$
expt[a]	0.21	79 ± 5	17 ± 6	4 ± 3
model **2**[b]	0.21	85	14	1
model **3**[b]	0.21	87	12	1
expt[a]	0.01	79 ± 20	17 ± 8	4 ± 3
model **2**[b]	0.01	9	65	26

[a] Accompanying paper 1 (ref 8). Expt averages over this time interval in kinetics models. [b] See Table 4 and text.

$NiC_3H_6^+ + H_2$ at long times. It may prove possible to more clearly discern such time-dependent branching effects in $Co^+ + C_3H_8$, for which much more H_2 is produced. Only about 3% of the total elimination products are formed at $t \geq 20$ μs.

Our experiment in effect integrates these rate curves over various time intervals, as described in detail in section II of paper 1. In Tables 5 and 6 we compare the model 2 results with experimental data. In integrating the model, we have properly averaged over the distribution of collision initiation times arising from the 8 μs delay between ion formation and extraction, as described in section II.A of paper 1. At 0.21 eV, the agreement between model and experiment is sensible for all measured quantities. In the mass spectrum collected with $t_{ext} = 8$ μs, the ratios of $NiC_2H_4^+$:$NiC_3H_6^+$:$NiC_3H_8^+$ intensities are 23:4:73 in the experiment and 21:4:75 from model 2. Further corroboration of the model comes from the Ni^+:$NiC_2H_4^+$:$NiC_3H_6^+$ ratio for delayed elimination products formed on longer time scales of 16−24 μs (Table 6). The experimental ratios are 79:17:4 compared with the ratios of 85:14:1 from model 2. The model predicts that some 80% of collision complexes have already dissociated back to reactants when we begin acquiring mass spectra at $t = 2-10$ μs. Unfortunately, in our experiment such Ni^+ ions cannot be distinguished from unreacted Ni^+ ions. Tables 5 and 6 show that model 3, which interchanges the roles of the initial bond insertion and multicenter transition states as described above, can also fit the time-resolved experimental data comparably well at $E_t = 0.21$ eV.

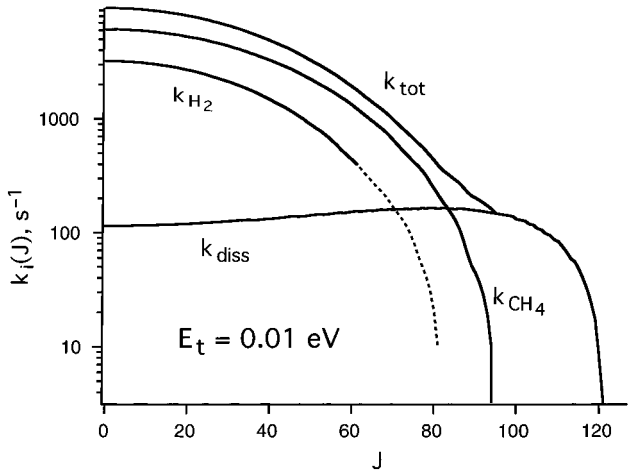

Figure 9. J dependence of k_{diss} and of the composite rates k_{CH_4} and k_{H_2} from eq 2 and model 2 at $E_t = 0.01$ eV. These calculations include no internal energy in reactants.

C. Additional Kinetic Energy and Isotope Effects. We must finally explore the effects of collision energy and isotopic substitution. In Figure 9, we show plots of the three parallel decay rates and of $k_{tot}(E,J)$ for the lower collision energy studied in the experiment, nominal $E_t = 0.01$ eV. These calculations include no internal energy in reactants. The decay rates plummet into the range 10^1-10^4 s^{-1}, which would be too slow for us to observe extensive complex decay on the time scale of our experiment, 0−25 μs. The return to reactants (k_{diss}) has shut down almost entirely, and k_{tot} is now dominated by elimination except at the very highest J.

Integration of the detailed decay rates vs t predicts that the experiment should see primarily intact complexes in the early time window $t \leq 10$ μs. Recall that the fraction of total products seen as CH_4 elimination in mass spectra taken at $t_{ext} = 8$ μs drops from 23% at $E_t = 0.21$ eV to 3% at nominal $E_t = 0.01$ eV. Model 2 predicts that only 2% of the complexes will have decayed in $t = 2-10$ μs, in sensible agreement with experiment (Table 5). However, the model predicts that those complexes that fragment in the longer time window 16−24 μs will form Ni^+:$NiC_2H_4^+$:$NiC_3H_6^+$ in the ratio 9:65:26, whereas we observe 79:17:4. If we add 1 and 2 kcal/mol of internal energy, the model ratios change to 44:42:14 and to 52:38:10, respectively, in somewhat better agreement with experiment. As we suggested in section III of paper 1, imperfections in the experimental selection of E_t or heating of the complexes during extraction may play a role here.

Finally, we explore the effects of deuterium isotopic substitution. We studied only $Ni^+ + C_3H_8$ in our time-resolved experiments. However, Armentrout and co-workers measured elimination cross sections as a function of E_t for the sequence C_3H_8, $CH_3CD_2CH_3$, $CD_3CH_2CD_3$, and C_3D_8.[11] At $E_t = 0.05$ eV, Table 7 reproduces the elimination reaction efficiencies σ_{elim}/σ_L and the branching fractions into the methane channel, summed over all CH_xD_{4-x} isotopomers. The predominant species observed is consistent with our model 2 (secondary insertion only, no scrambling) in all cases. For Ni^+, experiment finds that deuteration of only the central $-CH_2-$ group causes a modest 30% decrease in the cross section and has no effect on the branching fraction; the effect is even smaller for Co^+ and Fe^+. In contrast, deuteration of both $-CH_3$ groups (either $CD_3CH_2CD_3$ or C_3D_8) decreases the cross section by a factor

TABLE 7: Elimination Reaction Efficiency and Product Branching vs H/D Isotope Pattern at $E_t = 0.05$ eV

	σ_{elim}/σ_L				
		model **2**[b]		% methane elim	
reactant	expt[a]	$t = \infty$	$t = 500\ \mu$s	expt[a]	model **2**[b]
C_3H_8	0.13 ± 0.01	0.167	0.167	0.80 ± 0.02	0.83
$CH_3CD_2CH_3$	0.09 ± 0.01	0.158	0.158	0.82 ± 0.03	0.91
$CD_3CH_2CD_3$	0.04 ± 0.006	0.076	0.034	0.69 ± 0.02	0.66
C_3D_8	0.03 ± 0.005	0.057	0.011	0.73 ± 0.02	0.87

[a] Reference 11. [b] We integrate elimination products either to $t = \infty$ or only to $t = 500\ \mu$s to mimic the experimental conditions of ref 11. The percent methane elimination is insensitive to integration range.

TABLE 8: Differential Zero-Point Energy Effects (kcal/mol) of H/D Isotopic Substitution on Multicenter Transition States[a]

reactant	**MCTS**$_{CH_4}$	**MCTS**$_{H_2}$(2°)	**MCTS**$_{H_2}$(1°)
C_3H_8	0	0	0
$CH_3CD_2CH_3$	+0.2	+1.0	+1.0
$CD_3CH_2CD_3$	+1.3	+1.0	+1.1
C_3D_8	+1.5	+2.0	+1.9

[a] Each entry is the change in barrier height due to isotopic substitution (including zero-point effects) relative to the barriers given in Table 1 for the $Ni^+ + C_3H_8$ case.

of 3−4 and significantly enhances hydrogen elimination relative to methane. Roughly the same effects occur in Co^+ and Fe^+.

In adapting model 2 to the various isotopomers, we calculate a complete set of vibrational frequencies and moments of inertia for the key stationary points and proceed as before. Table 1 shows the energetic effects of perdeuteration as an example. Table 8 shows the differential zero-point effects of just the key MCTSs relative to reactants for all four isotopomers. Deuteration has only a very small effect on the relative energy of the complex **1** or of **TS$_{CC}$** and the CC insertion intermediate, as might be expected. The relative energy of **MCTS**$_{CH_4}$ increases by about 2 kcal/mol when both terminal $-CH_3$ groups are deuterated. In this reaction coordinate, one of the terminal hydrogens is migrating toward the metal atom. Interestingly, the energies of **MCTS**$_{H_2}$(**2**°) and **MCTS**$_{H_2}$(**1**°) increase by 1 kcal/mol on selective deuteration of both the terminal $-CH_3$ groups or of only the central $-CH_2-$ group. These same energies increase by 2 kcal/mol on deuteration of all groups. *Both* types of hydrogen are involved in the reaction coordinate, which has important implications for the interpretation of experimental isotope effects.

In model 2, deuteration at the terminal $-CH_3$ groups slows down the decay of the complex **1** to such a degree that a question of the time scale of observation arises in comparisons of cross sections with experiment. For example, at $E_t = 0.05$ eV, the model density of states of the $Ni(C_3D_8)^+$ complex, which scales k_{diss}, k_{CD_4}, and k_{D_2}, is 80 times larger than that of $Ni(C_3H_8)^+$ primarily due to lower vibrational frequencies. This results in overall decay rates k_{tot} in the $10^2-10^3\ s^{-1}$ range. With this in mind, in Table 7 we report the model reaction efficiencies and methane branching fractions for the different isotopomers at $E_t = 0.05$ eV. The reaction efficiencies are given for integration over two different assumed observation time windows: infinity and 500 μs. The latter is chosen to mimic Armentrout's actual experimental conditions.[43] The CH_4:H_2 branching is fairly insensitive to the assumed time window. Model 2 captures the observed dependence of cross section on deuteration of terminal $-CH_3$ groups reasonably well. The most important contribution is the primary isotope effect on the different barrier heights, but the time window is also significant. Armentrout reports that the fraction of overall products appearing as adducts at $E_t = 0.05$ eV increases substantially from C_3H_8 to C_3D_8, in accord with model 2. There is a real chance, for example, that some of the $Ni(C_3D_8)^+$ adducts would proceed to elimination products if observed for a sufficiently long time. For such long lifetimes, collisional or even radiative stabilization of the complexes might also become an issue.

D. Effects of High Exit-Channel Centrifugal Barrier on H_2 Elimination. In fitting model 2 to the data, it was necessary to adjust the energy of **MCTS**$_{H_2}$(**2**°) further downward than **MCTS**$_{CH_4}$ by 2 kcal/mol. One might hope that B3LYP produces *relative* TS energies to better accuracy than that. Therefore, we have examined the importance of two effects that might allow us to raise the energy of **MCTS**$_{H_2}$(**2**°). As suggested by van Koppen and Bowers,[10,11] the low mass and small polarizability of H_2 could make centrifugal effects particularly important in the exit channel of H_2 elimination paths. Thus far we have assumed that $J = l = l''$, where J is the total angular momentum, l is initial orbital angular momentum, and l'' is the orbital angular momentum at **TS$_{orb}$**″, the H_2 elimination exit channel barrier. That is, we have assumed no rotational excitation of the molecular products $NiC_3H_6^+ + H_2$. That caused us to cut off the range of J that contributes to the H_2 product at $J \le l''_{max}$, the largest l'' that can cross the barrier **TS$_{orb}$**″.

One possibility that might allow us to raise **MCTS**$_{H_2}$(**2**°) is tunneling of the light H_2 through the centrifugal barrier at **TS$_{orb}$**″, which might augment the curve marked k_{H_2} in Figure 6 by allowing higher J to penetrate **TS$_{orb}$**″. Miller has shown how to incorporate tunneling effects into the RRKM rate expression of eq 7 by running the state count $W^\dagger$(TS) over *all* states, including those with *less* energy in the reaction coordinate than the classical threshold.[44] Each entry in the state count is then weighted by the one-dimensional tunneling transmission probability, a number between 0 and 1. We carried out such calculations for $k_5^{exit}(E,J)$, the rate of passage from the exit well **5** over **TS$_{orb}$**″ to H_2 products. For each J, we fit the sum of the ion-induced dipole and the centrifugal potentials to an Eckart function,[34] for which the one-dimensional tunneling probability is available in closed form. However, the results indicate that tunneling is unimportant. Evidently, the centrifugal barrier is too thick. Figure 10 shows example calculations at $E_t = 0.21$ eV, assuming an H_2 exothermicity of 15 kcal/mol[32] and an exit-channel well depth of 35 kcal/mol.

Alternatively, we can reexamine the assumption that $J = l = l''$. Simple kinematics would indicate that much of the angular momentum present as overall rotation of the complex must remain as rotation of $NiC_3H_6^+$, since the center of mass of the complex and that of the $NiC_3H_6^+$ fragment nearly coincide. Nonzero j'' (rotation of fragments) will broaden the possible range of l'' for a given J, much as occurs in phase space theory. This might allow high-J complexes to dissociate to H_2 over relatively low angular momentum barriers, with j'' absorbing most of the total angular momentum J. The dashed line in Figure 6 shows the effect of including the maximum possible contribution of $J \ge l''_{max}$ in the H_2 product. Even if we assume that *every* J that crosses **MCTS**$_{H_2}$(**2**°) creates H_2, the effect on the H_2 branching fraction is modest. The reason is that, for higher J, k_{H_2} is a decreasing function of J while its competition, k_{diss}, is an increasing function of J. We estimate that even if all J that cross **MCTS**$_{H_2}$(**2**°) fully contribute to k_{H_2}, we would only be able to raise the barrier height by 0.6 kcal/mol.

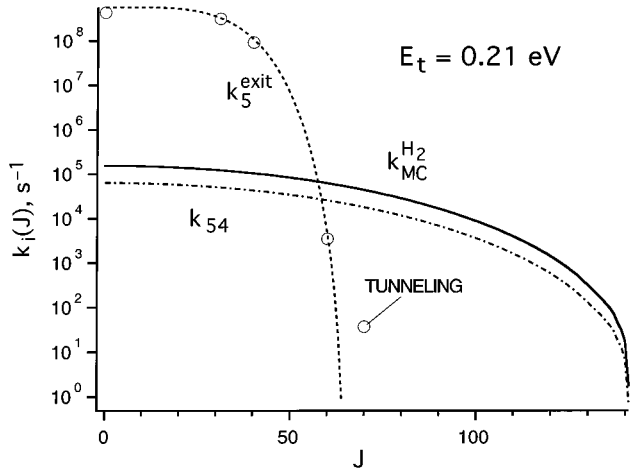

Figure 10. Example calculations of $k2^{H}_{MC}$, k_{54}, and $k_5^{exit}(E,J)$ from model 2 at $E_t = 0.21$ eV, assuming an H_2 exothermicity of 15 kcal/mol and an exit-channel well depth of 35 kcal/mol. The model for $k_5^{exit}(E,J)$ assumes that all angular momentum J becomes orbital angular momentum l'' at $\mathbf{TS_{orb}}''$. Open circles show slight enhancement of $k_5^{exit}(E,J)$ at high J by tunneling through the centrifugal barrier, using a simple one-dimensional model. See text.

Finally, for completeness, we examined the possibility that passage over $\mathbf{MCTS}_{H_2}(\mathbf{2}°)$ might be *reversible* even for moderate J, as k_5^{exit} becomes very slow. This would undermine a key assumption in the parallel, sequential decay model. For $J = 0-50$, the entire range that produces significant H_2 in the competition with other decay channels, Figure 10 shows that $k_5^{exit}(E,J)$ far exceeds $k2^{H}_{MC}$. In addition, $k2^{H}_{MC}$ is about a factor of 2 larger than k_{54} over the same range of J. These two comparisons validate the parallel, exponential decay model (eq 2), since passage over $\mathbf{MCTS}_{H_2}(\mathbf{2}°)$ is essentially never followed by return to the complex **1**, and the rate of production of H_2 is limited by $k2^{H}_{MC}$, not by $k_5^{exit}(E,J)$. However, if the barrier were significantly lower or if the internal energy were much higher, then k_{H_2} would compete more effectively with k_{CH_4} and k_{diss} and a significant fraction of the H_2 products might be produced at a rate limited by $k_5^{exit}(E,J)$, at least for high J. The real importance of this possibility depends on the detailed dynamics of H_2 elimination. For the CH_4 elimination channel, the analogous exit-channel effects are surely unimportant due to the heavier reduced mass and larger polarizability.

VI. Discussion

A. Summary of Preferred Model of the $Ni^+ + C_3H_8$ Reaction. We have had the advantage of building our statistical rate model 2 from the B3LYP vibrational frequencies and moments of inertia, which should be substantially more accurate than earlier ad hoc models. Within the adiabatic approximation, we have shown that a range of physically plausible models of the $Ni(C_3H_8)^+$ complex **1** and of $\mathbf{TS_{orb}}$ can fit the experimentally observed nanoseconds−microseconds decay times. If $\mathbf{TS_{orb}}$ is modeled as "loose", with free internal rotation of propane about the two axes perpendicular to the axis of approach, then it is necessary to "loosen" the model of **1** as compared to the crudest approximation of harmonic bending frequencies taken directly from the B3LYP calculations. We can then fit the experimental time scale by placing the $Ni^+-C_3H_8$ binding energy anywhere in the range 28.5−39.3 kcal/mol and varying the treatment of the soft modes of the complex.

A key mechanistic question is whether the MCTSs lie well above the bond insertion TSs or vice versa. Evidently very different sets of choices for the energies of $\mathbf{TS_{CC}}$, $\mathbf{MCTS}_{CH_4}$, $\mathbf{TS_{CH}}$, and $\mathbf{MCTS}_{H_2}(\mathbf{2}°)$ can produce a good elimination cross section at $E_t = 0.21$ eV and also time-integrated elimination branching fractions and time-dependent branching fractions in semiquantitative agreement with experiment. The experiments combined with statistical modeling cannot distinguish the possibilities. However, we strongly prefer model 2, which places each MCTS above the corresponding insertion TS, for two reasons. First, B3LYP theory makes a clear prediction that the MCTS is the highest potential energy point along each elimination pathway, as in our model 2. The same energetic ordering was found in B3LYP calculations on $Fe^+ + C_3H_8$.[14] Second, for the $Co^+ + C_3H_8$ reaction, recent isotopic labeling experiments by Armentrout and co-workers support the same conclusion.[42] They studied the two labeled reverse reactions $Co^+(C_3H_6) + D_2$ and $CoC_2H_4^+ + CD_4$ to make Co^+ + labeled propane in the ion beam apparatus. The reverse reactions to produce Co^+ are inefficient but observable. Importantly, what is *not* observed is isotopically scrambled reactants, e.g., $Co^+(C_3H_5D) + HD$ or $CoC_2H_3D^+ + CD_3H$. If, for example, $\mathbf{TS_{CH}}$ lay *above* $\mathbf{MCTS}_{H_2}(\mathbf{2}°)$, then in the $Co^+(C_3H_6) + D_2$ reaction we would expect the long-lived $Co^+(C_3H_6)(D_2)$ to cross and recross $\mathbf{MCTS}_{H_2}(\mathbf{2}°)$ many times before finally managing to cross $\mathbf{TS_{CH}}$ to produce $Ni^+(C_3H_6D_2)$ and then $Ni^+ + C_3H_6D_2$ very inefficiently. Multiple crossings of $\mathbf{MCTS}_{H_2}(\mathbf{2}°)$ would produce significant $Co^+(C_3H_5D) + HD$ scrambling product, which is not observed. The negative observation is easily explained if $\mathbf{MCTS}_{H_2}(\mathbf{2}°)$ lies above $\mathbf{TS_{CH}}$. Similar arguments hold for the CH_4 channel.

The potential energy profile of model 2 combines with centrifugal barrier effects that vary along the reaction coordinate to produce the following mechanistic picture. H_2 and CH_4 elimination arise only from low-J complexes (Figure 6). Even these low-J complexes must insert and deinsert many times before overcoming the high multicenter TS and eliminating H_2 or CH_4. At high J, the competition shifts to favor dissociation back to reactants, because k_{diss} is enhanced by orbital angular momentum while k_{CH_4} and k_{H_2} are diminished. High-J complexes also insert and deinsert, but they almost always return to $Ni^+ + C_3H_8$ reactants on a microsecond time scale. Due to the effects of angular momentum conservation, the overall decay of the $Ni(C_3H_8)^+$ population is nonexponential even for state- and energy-selected reactants.

Of course, the success of model 2 in explaining a wide range of experimental data does not prove the validity of the adiabatic hypothesis. It is not easy to see how to separate possible influences of excited electronic states from the many other uncertainties in an adiabatic model. It will be interesting to see whether comparable models with energies appropriately adjusted are equally successful for the Fe^+ and Co^+ reactions with C_3H_8, since these atoms have more 3d-shell vacancies and thus many more low-lying electronic states.

B. Accuracy of B3LYP Energetics. An important goal of this work is to assess the accuracy of the transition-state energies predicted by density functional theory. Model 2 achieves good semiquantitative agreement between statistical rate theory and a wide variety of experimental data by placing $\mathbf{MCTS}_{CH_4}$ at −2.5 kcal/mol and $\mathbf{MCTS}_{H_2}(\mathbf{2}°)$ at −2.2 kcal/mol, which is 5.6 and 7.2 kcal/mol, respectively, *below* the B3LYP results. We have explored the model space quite thoroughly. Within the class of models that place the MCTSs well above the corresponding bond insertion TSs, we estimate that the data constrain the energies of $\mathbf{MCTS}_{CH_4}$ and $\mathbf{MCTS}_{H_2}(\mathbf{2}°)$ to within ±2 kcal/mol. We have explored the effects of larger basis sets on the

B3LYP calculations, and it appears that all the calculated TSs would lie lower by only 1 kcal/mol if much larger basis sets could be used. We conclude that *if* statistical rate theory on a single potential energy surface provides an accurate description of the dynamics, then B3LYP *overestimates* the MCTS energies by about 5−7 kcal/mol. This discrepancy is somewhat larger than typical discrepancies of 3−5 kcal/mol between B3LYP and experimental bond dissociation energies of simple ligated metal species.[4] In the very different case of anionic S_N2 reactions in the gas phase, even larger discrepancies in barrier heights were found on comparing density functional theory with ab initio methods.[45]

The B3LYP exothermicities for CH_4 and H_2 elimination products disagree with the best experimental estimates by similar magnitudes, about 6 kcal/mol (Table 1 and footnotes). The sign of the discrepancy is in a sense opposite for the exothermicities (B3LYP energy of products lying below experimental estimate) and for the TSs (B3LYP energy lying above "experimental" estimates from data plus statistical modeling).

However, especially for the TSs, many subtleties and complications arise in comparing theory with experiment. One issue is the validity of the assumptions underlying RRKM theory, the adiabatic approximation, and the assumption of no recrossing trajectories at the multicenter transition states. Another issue is the internal energy distribution of reactants. Our experiment creates a beam of pure ground states, $Ni^+(3d^9,{}^2D_{5/2})$, and expands the propane through a pulsed nozzle, cooling it internally to an estimated mean energy below 1 kcal/mol. The excited $^2D_{3/2}$ level lies at 1506 cm^{-1} = 4.3 kcal/mol.[46] The theory has no spin−orbit interaction, so the B3LYP energies are referenced to a fictitious $(2J_{el} + 1)$-weighted average over spin−orbit levels, which lies at +565 cm^{-1} = +1.6 kcal/mol relative to the real $^2D_{5/2}$ level. Here $J_{el} = {}^5/_2$ is the electronic angular momentum of Ni^+. This suggests that the B3LYP MCTS energies may be too high by an additional 1.6 kcal/mol. As a further complication, other experiments include an unknown distribution of J_{el}, average over a broader range of propane internal energies, and may include even higher Ni^+ excited states as well. Another significant question is the treatment of reactant asymptotes by B3LYP. Ni^+ provides a nearly ideal test case, since B3LYP yields the correct energy difference between the $3d^84s(^4F)$ excited state and the $3d^9(^2D)$ ground state within 1.6 kcal/mol. It is important to extend these comparisons to Fe^+ and Co^+ reactions with alkanes to test the reliability of corrections for asymptotic energy errors. The differences encountered here underscore the importance of further, more refined experimental tests of the quantitative accuracy of density functional theory.

C. Multicenter Transition States and Agostic Interactions. B3LYP theory has provided new qualitative insights into the mechanisms of $M^+ + C_3H_8$ reactions by revealing the importance of multicenter transition states (MCTSs) along key elimination pathways. Earlier experimental work was interpreted in terms of a qualitatively different mechanism.[9−11] That mechanism involved initial CH or CC insertion over *rate-limiting* bond insertion TSs, followed by β-hydrogen or β-methyl migration to form rearrangement intermediates of structure $M^+(H)(CH_3)(C_2H_4)^+$ or $M^+(H)_2(C_2H_4)$, and then elimination of CH_4 or H_2. H_2 could form via two pathways, by initial primary or secondary CH bond insertion. CH_4 could also form in two ways, by initial primary CH insertion followed by β-methyl migration to the metal or by initial CC insertion followed by β-hydrogen migration. It has proven difficult to devise experiments that distinguish these possibilities. Armentrout, Bowers, and co-workers showed that the significant decrease in methane elimination cross section on deuteration is consistent with initial primary CH insertion and β-methyl migration.[10,11]

However, for Fe^+, Co^+,[12−14] and now Ni^+, modern electronic structure theory has consistently failed to find potential minima corresponding to the suggested $M^+(H)(CH_3)(C_2H_4)$ or $M^+(H)_2(C_2H_4)$ rearrangement intermediates. For Ni^+, with nine valence electrons, there are too few empty or singly occupied valence (3d and 4s) orbitals to form two σ bonds to H or alkyl *plus* a full donor−acceptor bond to ethylene. However, if valence configuration were the only consideration, we might expect Co^+ and Fe^+ (eight and seven valence electrons) to form the rearrangement intermediates more readily than Ni^+. Nevertheless, the calculations find very similar reaction paths for all three metal cations. Thus, it seems that *cations* from the right-hand side of the transition metal block do not form stable rearrangement intermediates. In a much simpler example, calculations predict that the ground state of FeH_2^+ is the molecular complex $Fe^+(H_2)$, rather than $H-Fe^+-H$.[12] In contrast, for the entire 4d series, PCI-80 calculations on reactions of *neutral* transition-metal atoms with C_2H_6 indeed found stable $M(H)_2C_2H_4$ intermediate potential wells en route to $MC_2H_4 + H_2$ elimination products.[7a] Evidently neutrals and ions find qualitatively different paths to the same H_2 elimination products. The ability of the cation to bind significantly to closed-shell molecules seems to drive these mechanistic differences.

For the M^+ cations, B3LYP theory finds that initial CH or CC bond insertion occurs over a *low* barrier; insertion intermediates of the form $H-M^+-C_3H_7$ or $CH_3-M^+-C_2H_5$ lie in shallow wells far below M^+ + alkane reactants. It had been argued[10,11] that the barrier to CC insertion should be much higher than the barrier to CH insertion, although the CC bond energy is only 88 kcal/mol compared with 101 kcal/mol for primary CH and 99 kcal/mol for secondary CH.[47] The argument involved better orbital overlap in the key transition states when using the spherical 1s orbital on H as compared with the more directional sp^x hybrid orbital on $-CH_3$. The orbital directionality effect seems to be significantly more important in neutral systems than in the cations studied here. Starting from the $Ni(C_3H_8)^+$ complex **1**, the B3LYP barriers to insertion $\mathbf{TS_{CH}}$ and $\mathbf{TS_{CC}}$ lie at very similar energies.

In the B3LYP results, the CH or CC insertion intermediate then rearranges to the deep exit-channel complex $M^+(H_2)(C_3H_6)$ or $M^+(CH_4)(C_2H_4)$ in concerted fashion over a high-energy MCTS. According to theory, these MCTSs are the highest points along the lowest energy paths to H_2 or alkane elimination in the reactions of Fe^+ with C_2H_6 and C_3H_8, of Co^+ with C_2H_6 and C_3H_8 and now of Ni^+ with C_2H_6, C_3H_8, and n-C_4H_{10}. It will be interesting to see whether this mechanism also holds for cations from the left-hand side of the transition-metal block, where electron−electron repulsion is much less severe. The geometries of the key MCTSs (Figure 3 and ref 14) suggest that *agostic interactions*[22] may play an important role in the relative stability of the various MCTSs, as suggested earlier by Holthausen and Koch.[12−14] Agostic bonds can be viewed as a kind of "preinsertion" complex involving donor−acceptor interactions, analogous to hydrogen bonding. A σ_{CH} bond donates electron density into an empty metal orbital of the proper symmetry; an occupied metal orbital may also donate electron density into σ_{CH}*. The CH bond lengthens. Similar agostic interactions evidently also help to stabilize the entrance- and exit-channel complexes.

For $Ni^+ + C_3H_8$, B3LYP finds that the key MCTSs lie at +3.1 kcal/mol for $\mathbf{MCTS}_{CH_4}$ (following initial CC insertion),

+5.0 kcal/mol for $\mathbf{MCTS}_{H_2}(\mathbf{2}°)$ (secondary CH insertion), and +11.4kcal/mol for $\mathbf{MCTS}_{H_2}(\mathbf{1}°)$ (primary CH insertion). Part of the reason for this energy ordering may lie in the quality of agostic bonds available between the metal cation and CH bonds of a nearby methyl group, as judged by variations in the three methyl CH bond lengths (Figure 3). In $\mathbf{MCTS}_{CH_4}$, there are two modest agostic interactions with the α-methyl group, whose σ bond to the metal is being broken in the TS. In $\mathbf{MCTS}_{H_2}(\mathbf{2}°)$, there is one very strong agostic interaction with the β-methyl group, which is otherwise uninvolved in the rearrangement. In contrast, $\mathbf{MCTS}_{H_2}(\mathbf{1}°)$ shows no evidence of agostic interactions, evidently because neither an α- nor a β-methyl group is available. The mechanistically important 5 kcal/mol energy difference between $\mathbf{MCTS}_{H_2}(\mathbf{2}°)$ and $\mathbf{MCTS}_{H_2}(\mathbf{1}°)$ might reasonably be attributed partly to the 2 kcal/mol difference in CH bond energies and partly to the strong agostic interaction in $\mathbf{MCTS}_{H_2}(\mathbf{2}°)$. According to the model, this difference is more than enough to steer *all* of the CH insertion along the secondary path, at least at low energy. Similar reasoning suggests that the low energy of $\mathbf{MCTS}_{CH_4}$ is primarily due to the weakness of the CC bond compared with CH, since the agostic interactions in this TS seem relatively weak.

The presence of strong agostic interactions in the entrance- and exit-channel complexes also helps to explain why the B3LYP binding energies of Ni^+ to C_3H_8 and *n*-C_4H_{10} are quite similar. The calculated binding energies do not scale with molecular polarizability. These local, geometry-specific interactions may be comparably important to the nonspecific ion-induced dipole binding mechanism that is so often invoked. It will be worthwhile to follow up on these qualitative observations with detailed model calculations that test the quantitative energetic importance of agostic interactions.

Another important conclusion from B3LYP theory is that β-methyl migration is intrinsically a high-energy process. At least for Ni^+ and Fe^+, theory clearly indicates that at low energy $M^+ + C_3H_8$ produces CH_4 elimination products exclusively by initial CC bond insertion, counter to earlier inferences. The alternative pathway involving *β-methyl* migration following primary CH insertion leads to the very high +16.8 kcal/mol barrier $\mathbf{MCTS}_{CH_4}(\mathbf{1}°)$.

D. Kinetic Energy Release Distributions (KERDs). Finally, we must discuss a set of experimental data that model 2 *cannot* explain. In earlier experimental work on the reactions of Fe^+, Co^+, and Ni^+ with C_3H_8, Bowers and co-workers presented measurements of kinetic energy release distributions (KERDs) in *both* the CH_4 and H_2 channels from metastable decay of long-lived $M^+(C_3H_8)$ complexes.[10,11] In all three reactions, the $MC_2H_4^+$ (+CH_4) KERDs are peaked near zero energy but *colder* than the predictions of phase space theory. This was nicely explained by invoking $\mathbf{TS_{CH}}$ as the rate-limiting barrier to *both* H_2 and CH_4 elimination. The latter must then involve β-methyl migration, a pathway now discredited by B3LYP calculations. Nevertheless, statistical modeling of the CH_4 KERD placed $\mathbf{TS_{CH}}$ at −2.3 ± 0.7 kcal/mol, just *below* reactants. This is remarkably similar to our best adjusted energy of −2.5 kcal/mol for $\mathbf{MCTS}_{CH_4}$, which plays the analogous role in our model 2. The colder-than-statistical CH_4 KERD was explained by the centrifugal barrier atop $\mathbf{TS_{CH}}$, which cuts off the range of orbital angular momentum J that can reach CH_4 elimination products. This in turn diminishes the highest energy component. In a phase space theory of the energy release, large kinetic energy correlates with high l' at $\mathbf{TS_{orb}}'$ and thus with high J. We have not attempted to calculate KERDs from model 2, but it seems very likely that our placement of $\mathbf{MCTS}_{CH_4}$ would produce a KERD in good agreement with the measurements for CH_4. In model 2, $\mathbf{MCTS}_{CH_4}$ limits the CH_4 channel to $J \leq 157$; similarly, if we place $\mathbf{TS_{CH}}$ at −2.3 kcal/mol as in the earlier model and use the moments of inertia from B3LYP theory, the centrifugal barrier would cut the CH_4 channel off at $J \leq 147$. Thus, the new CH_4 mechanism via $\mathbf{MCTS}_{CH_4}$ can equally well explain the methane KERD.

The problem lies with the H_2 channel, for which the KERD is *bimodal*, with a much larger mean kinetic energy than statistical theory predicts. This occurs to varying degrees for the reactions of Fe^+, Co^+, and Ni^+ with C_3H_8. The bimodality in the KERD for H_2 is especially pronounced for Fe^+ and Co^+; the Ni^+ distribution shows a significant high-energy tail rather than a distinct peak. A disturbing feature of the KERD for the $NiC_3H_6^+ + H_2$ channel is that it extends to 1.4 eV, well beyond the estimated exothermicity of 0.75 eV.[32] For all three metals, the low-energy component of the H_2 KERD peaks near zero and is roughly statistical, but the high-energy component peaks at 0.5−0.7 eV and has a long tail. Intriguingly, the KERD for HD elimination from $M^+ + CH_3CD_2CH_3$ is bimodal with the low-energy peak enhanced relative to the high-energy peak. The KERD for HD from $M^+ + CD_3CH_2CD_3$ is also bimodal but with amplitudes *reversed*; now the high-energy peak is enhanced over the low-energy peak. The results are qualitatively similar for Fe^+, Co^+, and Ni^+, but the quantitative details differ.

This striking isotope effect for the HD KERD from $CH_3CD_2CH_3$ and from $CD_3CH_2CD_3$ led to the interesting suggestion that the low-energy component arises from initial insertion into a *primary* CH bond, while the high-energy component arises from initial insertion into a *secondary* CH bond. This is in accord with the expected primary isotope effect under the *assumption* that $\mathbf{TS_{CH}}$ is rate-limiting, an assumption now in clear disagreement with theory. Furthermore, that idea did not explain why primary CH insertion would give a roughly statistical energy release for both CH_4 and H_2, while secondary insertion would give a highly nonstatistical release for H_2.

Detailed interpretation of the HD KERDs from mixed isotopomers in terms of our model 2 would be difficult. $\mathbf{MCTS}_{H_2}(\mathbf{1}°)$ and $\mathbf{MCTS}_{H_2}(\mathbf{2}°)$ now lie much higher in energy than $\mathbf{TS_{CH}}(\mathbf{1}°)$ and $\mathbf{TS_{CH}}(\mathbf{2}°)$, so the isotope effect arises not in the initial bond insertion, which is facile for all isotope patterns, but in the passage over the relevant MCTS. Table 8 summarizes the effects of zero-point energy corrections on the key barrier heights. Model 2, which explains so much other data, provides no rationale for associating either the high-energy portion or the low-energy portion of the H_2 KERD with either the primary or secondary CH insertion pathway. Neither model 2 nor its predecessors sheds any light on the underlying reason for the high-energy, nonstatistical H_2 KERD consistently observed in Bowers' experiments.

The KERDs experiment may be difficult to interpret for two reasons which couple to each other. First, the electron impact source of M^+ creates excited electronic states which might contribute to the observed metastable decay, as was recently observed on the same apparatus for the reaction $V^+ + C_2H_4$.[48] Second, the experiment observes metastable decay occurring in a time window covering about $t = 6-64$ μs after initiation of the collision.[49] This suggests the *possibility* that the low-energy, near-statistical component of the H_2 KERD arises from reaction of ground-state M^+ via secondary CH bond insertion and passage over $\mathbf{MCTS}_{H_2}(\mathbf{2}°)$. Primary CH insertion remains unimportant for ground-state M^+ at thermal collision energy, consistent with model 2. The high-energy component of the

H_2 KERD might then arise from reaction of metastable electronically excited states M^{+}*. That would immediately explain why the high-energy tail of the H_2 KERD extends some 0.6 eV beyond the estimated exothermicity. For example, Ni^+ has metastable (even parity) excited states at $E_{el} = 0.21$, 1.2, and 1.7 eV.[46] The electron impact ionization definitely populates such Ni^{+}* states.[50] Complexes formed from excited-state reactants might well cross rapidly to the ground adiabatic surface described by model 2 and then be able to overcome both $\mathbf{MCTS}_{H_2}(\mathbf{2}°)$ and $\mathbf{MCTS}_{H_2}(\mathbf{1}°)$. This in turn allows for the possibility that the high-energy component of the H_2 KERD becomes sensitive to deuterium substitution at the secondary CH bonds, as observed. It is difficult to fill in further details without knowing the electronic-state distribution.

If we tentatively attribute the high-energy, nonstatistical H_2 KERD to reactions of excited states of M^+, then the *time scale* of the elimination becomes critical, since Bowers detects metastable decay only in the $t = 6-64$ μs window. Reactant *electronic* energy is different from collision energy in that it brings internal energy but no additional orbital angular momentum to the collision complex. Presume for the moment that M^{+*} reactants quickly cross to the same ground-state surface described by our model 2. They would have the same J distribution as ground-state reactants but a distribution of total internal energy centered about the nonzero electronic excitation energy. Bowers has argued that adducts formed from excited-state Ni^+ would not contribute to the KERD because the additional energy will cause elimination to occur much faster than the observation time window.[11] This is plausible for the CH_4 elimination channel, for which J_{max} is limited by $\mathbf{MCTS}_{CH_4}$ and escape from the exit-channel complex involves only a small centrifugal barrier. However, as discussed in section V.D, for the H_2 products the exit-channel centrifugal effects could be very large. Depending on the detailed dynamics, for sufficiently high J the appearance rate of H_2 may be determined not by $k_{tot}(E,J)$ as in eq 2 but by $k_5^{exit}(E,J)$, which decreases rapidly with J (Figure 10). It is then possible that H_2 products could appear on a very wide range of time scales. For reactions of excited states M^{+}*, the H_2 products arising from low-J collisions will surely tend to appear rapidly and would not contribute to the time window of the KERD measurements. The same is true of the CH_4 product from both M^+ and M^{+}* reactants. However, for any given M^{+}* energy up to about 3 eV, there could exist collision complexes with exit-channel centrifugal barriers just large enough (i.e., having just the right range of J) to cause H_2 to appear in the experimental time window of 6−64 μs.

This line of reasoning might explain how KERD peaked at high kinetic energy could arise from a statistical process. A statistical model *of only those excited-state complexes that emit H_2 within the 6−64 μs* detection window must average over an unusual J distribution peaked at large, nonzero J. Because of the correlation in phase space theory between high kinetic energy release and high J, the observed KERD due to M^{+}* might then *peak at nonzero kinetic energy*, as observed experimentally. In this idea, the experimental time window causes the observed H_2 KERD from electronically excited states to be depleted at *low* kinetic energy for roughly the same reason that the CH_4 KERD from the ground state were depleted at *high* kinetic energy. Both low-energy and high-energy features of the H_2 KERD might then arise from statistical decay on the ground adiabatic surface, but with different initial electronic energies. This could also explain why the metastable decay products show a significantly larger H_2:CH_4 ratio than other experiments.

Lacking the electronic-state distribution, it is difficult to explain in detail the sensitivity of the KERD to the pattern of deuterium substitution. However, we would surely need to invoke significant involvement of initial *primary* CH insertion at higher energy. At first glance, it seems that the 6.4 kcal/mol difference between $\mathbf{MCTS}_{H_2}(\mathbf{1}°)$ and $\mathbf{MCTS}_{H_2}(\mathbf{2}°)$ would preclude the primary pathway from ever competing with the secondary pathway. However, angular momentum conservation may again provide the answer. The two MCTSs differ substantially in their moments of inertia (Table 3). $\mathbf{MCTS}_{H_2}(\mathbf{2}°)$ has the larger rotational constants and thus larger centrifugal barrier for a given J. At higher energy, a larger range of J can cross $\mathbf{MCTS}_{H_2}(\mathbf{1}°)$ than $\mathbf{MCTS}_{H_2}(\mathbf{2}°)$; for example, our calculations show that for $E_t = 1$ eV this effect causes the primary CH path to overcome the secondary CH path in its overall contribution to the H_2 elimination product.

This qualitative argument has been highly speculative. It remains uncertain how the combined effects of electronic energy, collision energy, orbital angular momentum, and the experimental time window might play out in a real experiment. The key open question seems to be the extent to which orbital angular momentum constraints in the $NiC_3H_6^+ + H_2$ exit channel might produce a broad range of H_2 appearance time scales from electronically excited reactants. Conservation of angular momentum certainly does not require high-J complexes to eject H_2 over a large orbital angular momentum barrier, since j'' (rotation of $NiC_3H_6^+$) might well absorb most of the angular momentum. Both the kinematics of the unusual mass combination and real dynamical constraints may be important. Nevertheless, our speculations at least provide the possibility that a single, comprehensive model of $Ni^+ + C_3H_8$ reacting on the adiabatic ground electronic surface might explain *all* of the experimental data. New measurements of KERDs for collisions of pure ground-state M^+ and of specific excited states are clearly needed. We hope to carry out such measurements by time-of-flight on the crossed-beam machine described in paper 1.

VII. Summary and Conclusion

The combination of electronic structure theory, statistical rate theory, and a variety of experimental measurements provides a remarkably detailed view of the $Ni^+ + C_3H_8$ reaction. Our new model 2, based on B3LYP calculations, consistently places multicenter transition states at the highest points along each elimination pathway, far higher than the corresponding bond insertion transition states. Such a model can readily explain all the data previously explained by the traditional stepwise model of the reaction, in which bond insertion transition states were rate-limiting. It appears that agostic interactions between Ni^+ and CH bonds of nearby methyl groups may play a key role in the stability of the multicenter transition states and that these may be a characteristic feature of transition-metal *cation* reaction pathways. Theory strongly suggests that neutral and cationic transition-metal atoms react with alkanes to eliminate H_2 via qualitatively different pathways.

It is important to continue to test statistical theory against experiment. We plan to extend this work to the $Ni^+ + n$-C_4H_{10} reaction to the reactions of Co^+ with C_3H_8 and n-C_4H_{10}. It will be informative to see whether modeling choices similar in spirit to those explored here will be comparably successful in treating larger or electronically more complex reactions.

Acknowledgment. J.C.W. thanks the National Science Foundation (CHE-9616724) and the donors of the Petroleum Research Foundation (PRF-31202-AC6) for generous support

of this research. S.S.Y. acknowledges support from a Lubrizol Fellowship. We thank Prof. P. B. Armentrout, Prof. M. T. Bowers, and Dr. P. A. M. van Koppen for many stimulating interactions.

References and Notes

(1) Bauschlicher, C. W.; Langhoff, S. R.; Partridge, H. In *Modern Electronic Structure Theory*; Yarkony, D. R., Ed.; World Scientific Publishing Company: London, 1995. Siegbahn, P. E. M.; Blomberg, M. R. A. *J. Am. Chem. Soc.* **1992**, *114*, 10548. Blomberg, M. R. A.; Siegbahn, P. E. M.; Svensson, M.; Wennerberg, J. In *Energetics of Organometallic Species*; Martinho Simões, J. A., Ed.; Kluwer Academic Publishers: Dordrecht, 1992. Musaev, D. G.; Morokuma, K.; Koga, N.; Nguyen, K. A.; Gordon, M. S.; Cundari, T. R. *J. Phys. Chem.* **1993**, *97*, 11435. Siegbahn, *Adv. Chem. Phys.* **1996**, *93*, 333.

(2) Siegbahn, P. E. M.; Blomberg, M. R. A.; Svensson, M. *Chem. Phys. Lett.* **1994**, *223*, 35. Siegbahn, P. E. M.; Svensson, M.; Boussard, P. E. J. *J. Chem. Phys.* **1995**, *102*, 5377.

(3) Becke, A. D. *J. Chem. Phys.* **1993**, *98*, 1372.

(4) (a) Blomberg, M. R. A.; Siegbahn, P. E. M.; Svensson, M. *J. Chem. Phys.* **1996**, *104*, 9546. (b) Wittborn, C. A. M.; Costas, M.; Blomberg, M. R. A.; Siegbahn, P. E. M. *J. Chem. Phys.*, in press.

(5) Eller, K.; Schwarz, H. *Chem. Rev. (Washington, D.C.)* **1991**, *91*, 1121. Armentrout, P. B. In *Selective Hydrocarbon Activation: Principles and Progress*; Davies, J. A., Watson, P. L., Greenberg, A., Liebman, J. F., Eds.; VCH: New York, 1990. Beauchamp, J. L.; van Koppen, P. A. M. In *Energetics of Organometallic Species*; Martinho Simões, J. A., Ed.; Kluwer Academic Publishers: Dordrecht, 1992. Weisshaar, J. C. In *State-Selected and State-to-State Ion−Molecule Reaction Dynamics*; Ng, C. Y., Ed.; Wiley: New York, 1992. *Organometallic Ion Chemistry*; Freiser, B. S., Ed.; Kluwer Academic Publishers: Dordrecht, The Netherlands, 1996.

(6) Weisshaar, J. C. In *Laser Chemistry of Organometallics*; Chaiken, J., Ed.; American Chemical Society: Washington, DC, 1993.

(7) (a) Carroll, J. J.; Haug, K. L.; Weisshaar, J. C.; Blomberg, M. R. A.; Siegbahn, P. E. M.; Svensson, M. *J. Phys. Chem.* **1995**, *99*, 13955. (b) Carroll, J. J.; Weisshaar, J. C.; Siegbahn, P. E. M.; Wittborn, C. A. M.; Blomberg, M. R. A. *J. Phys. Chem.* **1995**, *99*, 14388.

(8) Noll, R. J.; Yi, S. S.; Weisshaar, J. C. *J. Phys. Chem. A* **1998**, *102*, xxxx (preceding paper 1).

(9) Hanratty, M. A.; Beauchamp, J. L.; Illies, A. J.; van Koppen, P. A. M.; Bowers, M. T. *J. Am. Chem. Soc.* **1988**, *110*, 1.

(10) van Koppen, P. A. M.; Brodbelt-Lustig, J.; Bowers, M. T.; Dearden, D. V.; Beauchamp, J. L.; Fisher, E. R.; Armentrout, P. B. *J. Am. Chem. Soc.* **1991**, *113*, 2359.

(11) van Koppen, P. A. M.; Bowers, M. T.; Fisher, E. R.; Armentrout, P. B. *J. Am. Chem. Soc.* **1994**, *116*, 3780.

(12) Holthausen, M. C.; Fiedler, A.; Schwarz, H.; Koch, W. *J. Phys. Chem.* **1996**, *100*, 6236.

(13) Holthausen, M. C.; Koch, W. *J. Am. Chem. Soc.* **1996**, *118*, 9932.

(14) Holthausen, M. C.; Koch, W. *Helv. Chim. Acta* **1996**, *79*, 1939.

(15) Casey, C. P.; Vosejpka, P. C.; Underiner, T. L.; Slough, G. A.; Gavney, J. A. *J. Am. Chem. Soc.* **1993**, *115*, 6680.

(16) Troe, J. *J. Chem. Soc., Faraday Trans.* **1994**, *90*, 2303.

(17) Aubanel, E. E.; Wardlaw, D. M.; Zhu, L.; Hase, W. L. *Int. Rev. Phys. Chem.* **1991**, *10*, 249.

(18) Booze, J. A.; Schweinsberg, M.; Baer, T. *J. Chem. Phys.* **1993**, *99*, 4441.

(19) Robinson, P. J.; Holbrook, K. A. *Unimolecular Reactions*; Wiley-Interscience: New York, 1972.

(20) Gilbert, R. G.; Smith, S. C. *Theory of Unimolecular and Recombination Reactions*; Blackwell Scientific Publications: Oxford, UK, 1990.

(21) Baer, T.; Hase, W. L. *Unimolecular Reaction Dynamics*; Oxford University Press: New York, 1996.

(22) Brookhart, M.; Greem, M. L. H. *J. Organomet. Chem.* **1983**, *250*, 395. Grubbs, R. H.; Coates, G. W. *Acc. Chem. Res.* **1996**, *29*, 85.

(23) GAUSSIAN 94: Frisch, M. J.; Trucks, G. W.; Schlegel, H. B.; Gill, P. M. W.; Johnson, B. G.; Robb, M. A.; Cheeseman, J. R.; Keith, T. A.; Petersson, G. A.; Montgomery, J. A.; Raghavachari, K.; Al-Laham, M. A.; Zakrzewski, V. G.; Ortiz, J. V.; Foresman, J. B.; Cioslowski, J.; Stefanov, B. B.; Nanayakkara, A.; Challacombe, M.; Peng, C. Y.; Ayala, P. Y.; Chen, W.; Wong, M. W.; Andres, J. L.; Replogle, E. S.; Gomperts, R.; Martin, R. L.; Fox, D. J.; Binkley, J. S.; Defrees, D. J.; Baker, J.; Stewart, J. P.; Head-Gordon, M.; Gonzalez, C.; Pople, J. A. Gaussian, Inc., Pittsburgh, PA, 1995.

(24) (a) Hay, P. J.; Wadt, W. R. *J. Chem. Phys.* **1985**, *82*, 299. (b) Dunning, T. H., Jr.; Hay, P. J. In *Modern Theoretical Chemistry*; Schaefer, H. F., III Ed.; Plenum: New York, 1976; pp 1−28.

(25) Wachters, A. J. H. *J. Chem. Phys.* **1970**, *52*, 1033.

(26) Lee, C.; Yang, W.; Parr, R. G. *Phys. Rev. B* **1988**, *37*, 785.

(27) Vosko, S. H.; Wilk, L.; Nusair, M. *Can. J. Phys.* **1980**, *58*, 1200.

(28) Pople, J. A.; Head-Gordon, M.; Fox, D. J.; Raghavachari, K.; Curtiss, L. A. *J. Chem. Phys.* **1989**, *90*, 5622.

(29) Perdew, J. P.; Wang, Y. *Phys. Rev. B* **1992**, *45*, 3244.

(30) Ricca, A.; Bauschlicher, C. W. *Chem. Phys. Lett.* **1995**, *245*, 150.

(31) Chong, D. P.; Langhoff, S. R. *J. Chem. Phys.* **1986**, *84*, 5606.

(32) Reference 11 gives the exothermicities of the CH_4 and H_2 elimination channels as 1.11 and 0.65 eV, respectively. We used these values to calculate the range of J that can surmount exit channel barriers. More accurate estimates based on recent collision-induced dissociation experiments are 1.09 and 0.67 eV (Sievers, M. R.; Jarvis, L. M.; Armentrout, P. B. Manuscript in preparation). The range of J depends only very weakly on which estimate is used.

(33) Gioumousis, G.; Stevenson, D. P. *J. Chem. Phys.* **1958**, *29*, 294.

(34) Johnston, H. S. *Gas-Phase Reaction Rate Theory*; The Ronal Press: New York, 1966.

(35) Duffy, L. M.; Keister, J. W.; Baer, T. *J. Phys. Chem.* **1995**, *99*, 17862.

(36) Perry, J. K.; Ohanessian, G.; Goddard, W. A. *J. Phys. Chem.* **1993**, *97*, 5238.

(37) *CRC Handbook of Chemistry and Physics*; 75th ed.; Lide, D. R., Ed.; CRC Press: Boca Raton, FL, 1995.

(38) Beyer, T.; Swinehart, D. F. *Commun. ACM* **1973**, *16*, 379.

(39) Bieske, E. J.; Rainbird, M. W.; Knight, A. E. W. *J. Chem. Phys.* **1991**, *94*, 7019.

(40) Pechukas, P. In *Dynamics of Molecular Collisions*; Miller, W. H., Ed.; Plenum Press: New York, 1976.

(41) Mitchell, S. A. In *Gas-Phase Metal Reactions*; Fontijn, A., Ed.; Elsevier: Amsterdam, 1992.

(42) Haynes, C. L.; Fisher, E. R.; Armentrout, P. B. *J. Phys. Chem.* **1996**, *100*, 18300.

(43) Estimated from the experimental flight path. The experimental time window depends on the kinetic energies of ions, and it is roughly 100 μs for energies near 1 eV. See: Ervin, K. M.; Armentrout, P. B. *J. Chem. Phys.* **1985**, *83*, 166.

(44) Miller, W. H. *J. Am. Chem. Soc.* **1979**, *101*, 6810.

(45) Deng, L.; Branchadell, V.; Ziegler, T. *J. Phys. Chem.* **1994**, *98*, 10645.

(46) Sugar, J.; Corliss, C. *J. Phys. Chem. Ref. Data* **1985**, *14* (Suppl. 2). Fuhr, J. R.; Martin, G. A.; Wiese, W. L. *J. Phys. Chem. Ref. Data* **1988**, *17* (Suppl. 4).

(47) Lias, S. G.; Bartmess, J. E.; Liebman, J. F.; Holmes, J. L.; Levin, R. D.; Mallard, W. G. *J. Phys. Chem. Ref. Data* **1988**, *17*.

(48) Gidden, J.; van Koppen, P. A. M.; Bowers, M. T. *J. Am. Chem. Soc.* **1997**, *119*, 3935.

(49) The range of residence time of complexes in the ion source is 0−50 μs (van Koppen, P. A. M. Personal communication). Complexes decompose between 6 and 14 μs after exiting the ion source. See ref 11.

(50) Kemper, P. R.; Bowers, M. T. *J. Phys. Chem.* **1991**, *95*, 5134.